Light Scattering and Rheology of Complex Fluids Driven far from Equilibrium

David J. Pine

August 13, 2001

1 Introduction

In these lectures, we explore two examples of systems driven far from equilibrium by the application of shear. With these two examples, we investigate different experimental strategies which are designed to directly probe the connection between macroscopic non-linear rheology and the microscopic structure and dynamics of a broad range of soft materials. The study of these systems illustrate the importance of performing *simultaneous* measurements of the microscopic structure, flow, and rheological properties of soft materials when such systems are driven far from equilibrium by shear flows. There are several reasons for this. First, the flows are frequently inhomogeneous. Such inhomogeneities can arise from various mechanisms; the two most frequently observed and discussed are hydrodynamic instabilities and flow-induced phase transitions. Other difficulties can also arise for the case of virtually any flow that is not a pure shear flow. In pure extensional flows, for example, the nonlinear rheological properties of the fluid under study can modify the flow field in ways that are extremely difficult to predict. Thus, without a detailed knowledge of the flow field, it is virtually impossible to develop a meaningful theory. Second, systems do not always tend towards a steady state. And even when they do, the steady state is not necessarily characterized by any general principle of detailed balance to constrain the theory which one can construct. Furthermore, the structures that develop under shear often do not resemble the structures found in the same system in equilibrium. That is, the nonequilibrium structures frequently cannot be described as perturbations of the equilibrium structures. Therefore, as important as microscopic structural measurements are for understanding and developing theories for systems in equilibrium, they become even more important when systems are driven far from equilibrium.

The systems we study are solutions of worm-like micelles and oil-in-water emulsions. These two systems exhibit many of the generic properties that soft materials exhibit under shear flow including a shear-induced phase transition, inhomogeneous flows, plastic deformation, and yielding. We explore these phenomena in these two systems with a combination of optical and light scattering techniques, and with rheological measurements.

In the first section, we review some important aspects of basic light scattering theory. We then discuss some general characteristics of light scattering when the system under study is subjected to a steady or oscillatory shear flow. We conclude our discussion of

light scattering with an overview of diffusing-wave spectroscopy (DWS), that is, dynamic light scattering (DLS) in the multiple scattering limit.

Next, we discuss the results of some recent experiments on shear thickening in dilute and semi-dilute solutions of wormlike micellar solutions. We also present a phenomenological theory for shear thickening in these systems which captures many of the salient features of our experiments. Our discussion of the experiments and theory is preceded by a brief overview of wormlike micellar solutions.

Finally, we present results from some recent experiments which examine microstructural changes in dense glassy emulsions when they are sheared beyond the limit of linear response.

2 Light and other scattering techniques

Scattering techniques are among the most powerful and widely used methods for probing the microscopic structure and dynamics of matter. In soft condensed matter, the most commonly used scattering techniques are X-ray, neutron, and light scattering. The choice of which scattering technique to use depends first and foremost on the length scale of the structures that one wishes to probe. The length scales directly probed by the various scattering techniques are set by the wavelength of the radiation. The smallest length scale that can be directly measured by scattering is $\lambda/2$ where λ is the wavelength of the radiation. As discussed later, larger length scales are probed by varying the scattering angle. For x-ray and neutron scattering, where the wavelengths used are typically ~ 1 Å, the upper limit is about 1000 Å, which can be achieved by working at very small scattering angles. For light scattering, where the wavelength is ~ 0.5 μm, the upper limit us usually several microns although length scales of up to ~ 200 μm have been achieved recently.

Another consideration in choosing which scattering technique to use has to do with how the radiation interacts with matter. X-rays are scattered by fluctuations in the electron density. Therefore, substances containing heavier elements scatter more strongly than substances rich in the lighter elements. For example, substances containing a great deal of hydrogen and relatively low concentrations of heavier elements scatter x-rays weakly. By contrast, neutrons interact primarily through the nuclear interaction, which varies more or less randomly from one nuclear species to another. It so happens that neutrons are scattered by hydrogen much more strongly than are x-rays. In fact, scattering from hydrogen and its heavier isotope, deuterium, scatter in such a way that they partially cancel one another. Thus, by judiciously adjusting the concentration and location of hydrogen and deuterium within a molecule, one can adjust the overall scattering strength and even selectively scatter from hydrogen atoms at specific molecular locations. Such "contrast matching" has proven to be a powerful tool for probing the structure of polymers and other complex fluids. Neutrons also have magnetic moments and therefore couple to the spin of nuclei. Thus, systems with magnetic properties can be probed with neutrons. By contrast, light is scattered by fluctuations in the dielectric constant of a material. Light is an especially useful probe of soft materials because they frequently contain structures with length scales comparable to the wavelength of light. In fact, the "softness" of many and perhaps even most soft materials is derived from the fact that they are made up of structures whose fundamental length scales is comparable to optical length scales.

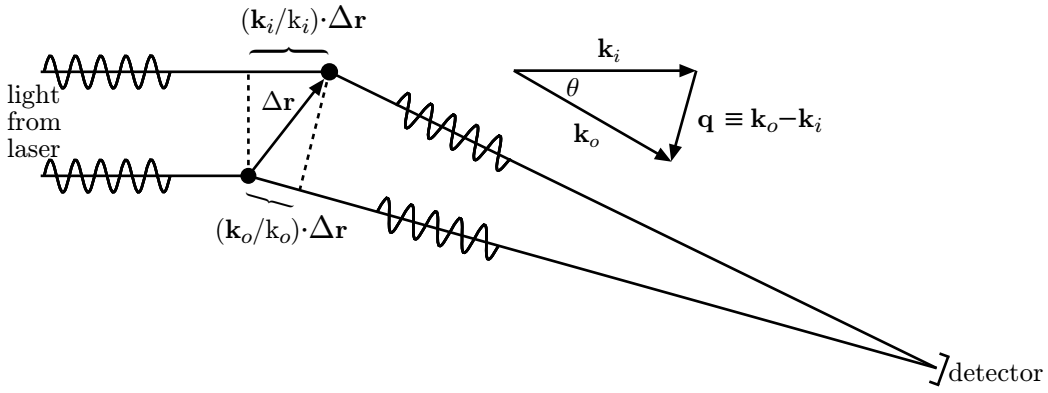

Figure 1: Schematic for scattering of light from two particles.

One other characteristic of light scattering that bears mentioning is that light is typically is scattered much more strongly than are x-rays or neutrons. A simple quantitative measure of the scattering strengths of light and x-rays is mean spatial fluctuation in the dielectric $\Delta\epsilon/\epsilon$. For a typical sample probed by light scattering $\Delta\epsilon/\epsilon \sim 0.1$; for x-ray scattering $\Delta\epsilon/\epsilon \sim 10^{-5}$. Thus, light is scattered much strongly than are x-rays (neutron scattering strengths are roughly comparable to x-rays). One consequence of this is that multiple scattering is frequently an important consideration for light scattering experiments whereas it is almost never important for x-ray or neutron scattering. In fact, multiple scattering is such a common occurrence in light scattering experiments that techniques have been developed to cope with and in some cases even exploit multiple light scattering. Further on in these lectures, we will discuss diffusing-wave spectroscopy (DWS), a technique which exploits multiple light scattering to probe very small particle movements. We now turn to a discussion of basic light scattering theory.

2.1 Static light scattering

The basic principles of light scattering can be understood by first considering scattering from two nearby particles as illustrated in Figure 1. Coherent light from a laser is incident from the left onto the two particles. Light scattered through an arbitrary scattering angle θ is collected by a detector which is sensitive to the *intensity* of the light that falls on its surface. Light scattered from the top particle will in general have traveled a different distance from the laser to the detector than will have the bottom particle. Thus, the scattered electric fields from the two particles will not be in phase with each other. Since the wavelength of the scattered light is unchanged (*i.e.* the scattering is elastic), the difference in phase is given by the wavevector $k \equiv 2\pi/\lambda$ times the difference in path lengths Δs, where λ is the wavelength of light in sample. From Figure 1, the difference in path lengths is $\Delta s = (\mathbf{k}_o/k_o)\cdot\Delta\mathbf{r} - (\mathbf{k}_i/k_i)\cdot\Delta\mathbf{r}$. In writing down this expression for Δs, we have made the approximation that the distance between particles is small compared to the distance between the particles and the detector. Thus, the paths from each of the two particles to the detector are essentially parallel. This is usually an excellent approximation. Noting that $k \equiv k_i = k_o$, the phase difference $\Delta\phi$ is

$$\Delta\phi \;=\; k\Delta s = (\mathbf{k}_o - \mathbf{k}_i)\cdot\Delta\mathbf{r}$$

$$= \quad \mathbf{q} \cdot \Delta \mathbf{r} \; , \tag{1}$$

where the scattering vector is defined by $\mathbf{q} \equiv \mathbf{k}_o - \mathbf{k}_i$. Clearly, if $\Delta\phi \sim \pi$, the light scattered from the different particles interferes destructively. If $\Delta\phi \sim 0$, the scattered light interferes constructively. Thus, the relative phase between the light scattered from different particles is sensitive to particle positions on the length scale of the wavelength of light. This is the essential physics which underlies the sensitivity of light scattering to the spatial structure of the scatterers. One additional note: as can be seen from the geometry of the scattering diagram in Figure 1, the magnitude of $\mathbf{q}$ is related to the scattering angle θ by

$$q = 2k \sin \frac{\theta}{2} \; . \tag{2}$$

To obtain a quantitative expression for the scattered intensity from N particles, we first add the contributions from all particles within the scattering volume to obtain the total electric field at the detector:

$$\begin{aligned} \mathbf{E}_d(\mathbf{q}) &= \sum_{i=1}^{N} \mathbf{E}_i e^{i\mathbf{q}\cdot\mathbf{r}_i} \\ &= \mathbf{E}_s \sum_{i=1}^{N} e^{i\mathbf{q}\cdot\mathbf{r}_i}; \end{aligned} \tag{3}$$

where the absolute phase for each path $\phi_i = \mathbf{q}\cdot\mathbf{r}_i$ is measured relative to an arbitrary fixed origin (as we will see below, the scattered intensity does not depend on the choice of the origin of the coordinate system). For simplicity, we have assumed that the amplitudes of the scattered fields $\mathbf{E}_i$ are all identical and equal to $\mathbf{E}_s$ as would be the case for identical spherical particles much smaller than the wavelength of light. The scattered *intensity* is proportional to the *square* modulus of the electric field:

$$\begin{aligned} I_d(\mathbf{q}) &\propto |E_d|^2 = |E_s|^2 \sum_{i=1}^{N} e^{i\mathbf{q}\cdot\mathbf{r}_i} \sum_{j=1}^{N} e^{-i\mathbf{q}\cdot\mathbf{r}_j} \\ &= |E_s|^2 \sum_{i,j}^{N} e^{i\mathbf{q}\cdot(\mathbf{r}_i - \mathbf{r}_j)} \; . \end{aligned} \tag{4}$$

Thus, it is apparent that the scattered intensity is proportional to the *relative* positions of the scatters and, as expected, is not sensitive to our choice of coordinate systems for calculating the phase of the scattered light. Static light scattering experiments measure the average of the scattered intensity. Therefore, it is useful to extract from the ensemble average of Eq. (4) that part which contains the structural information in which we are interested. To this end, we define the *static structure factor*,

$$S(\mathbf{q}) \equiv \frac{1}{n} \sum_{i,j}^{N} \left\langle e^{i\mathbf{q}\cdot(\mathbf{r}_i - \mathbf{r}_j)} \right\rangle \; , \tag{5}$$

and note that $I(\mathbf{q}) \propto S(\mathbf{q})$. The static structure factor $S(\mathbf{q})$ can be calculated without recourse to scattering theory as it contains only information about the average relative positions of particles. Thus, $S(\mathbf{q})$ is the quantity that connects static light scattering measurements with theory.

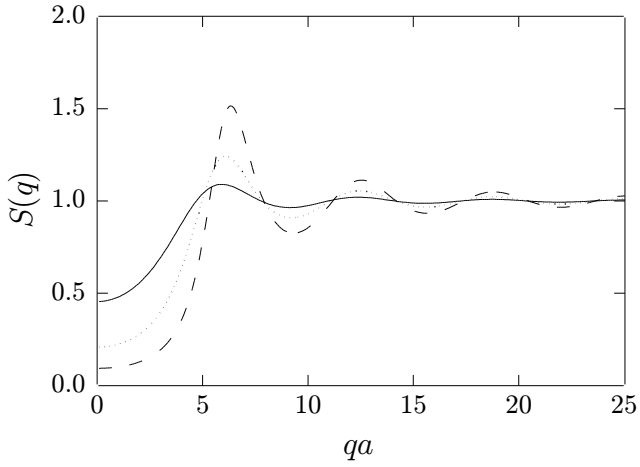

Figure 2: Static liquid structure factor for different volume fractions: solid line – $\phi = 0.1$; dotted line – $\phi = 0.2$; dashed line – $\phi = 0.3$ (calculated for hard spheres using the Percus-Yevick approximation).

2.1.1 Liquid structure factors

In order to develop some intuition about the results of scattering experiments, it is useful to consider a few examples. First, we consider scattering from a disordered liquid. In Figure 2, we show $S(q)$ for a liquid of hard spheres at three different volume fractions. Because a liquid is isotropic, the structure factor can only depend on the magnitude of q. We can better understand the origin of the oscillations in $S(q)$ by considering its relationship to the radial distribution function $g(r)$,

$$S(q) = 1 + n \int_V d\mathbf{r}\; g(r)\; e^{i\mathbf{q}\cdot\mathbf{r}}\;, \tag{6}$$

where $n = N/V$ is the average particle density. Physically, $n\,g(r)$ can be thought of as the average density of particles a distance r from the center of an arbitrary particle. Thus, if we consider the spatial structure of a liquid as illustrated in Figure 3, we see that $g(r)$ must be zero near the origin since no other particle can occupy the same space as our reference particle out to some finite distance roughly comparable to the particle diameter. At a radius corresponding to the first coordination shell, there is a higher than average probability of finding another particle so $g(r)$ must exceed unity. Between the first and second coordination shells, the density will again fall below the average density in a dense liquid because of packing constraints. At the second coordination shell, $g(r)$ will once again rise above unity but not as high as the first peak. This diminishing of the height of the peaks (and depth of the valleys) as the distance from the center of the labeled particle increases arises because the correlations in the particle positions die off due to the accumulation of space in which particle positions can fluctuate relative to a central labeled particle. At large distances, all correlations die off in a liquid and $g(r)$ tends towards unity. The static structure factor $S(q)$ is, according to Eq. (6), the Fourier transform of $g(r)$. Therefore, we can understand the origin of the oscillations in $S(q)$ at finite q as merely reflecting the short-range correlations between particles due primarily to packing constraints arising from the repulsive core of the potential. Thus, the first peak in $S(q)$ occurs in the vicinity of $2\pi/d$ where d is the range of the repulsive potential. The

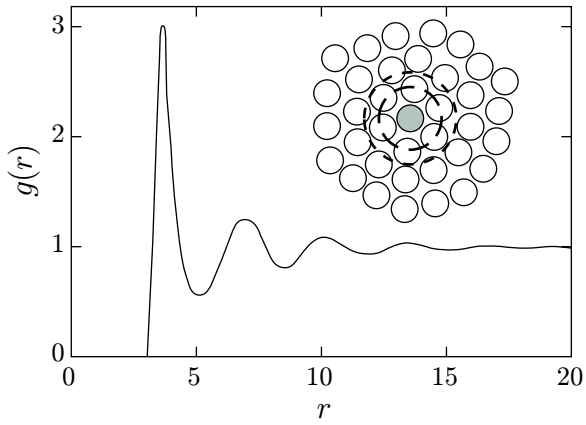

Figure 3: Radial distribution function $g(r)$ and real space distribution of particles (inset). Dashed circles indicate the location of the first peak (long dashes) and first minimum (short dashes.

structure factor is most interesting for diatomic and more complex molecules, as well as for mixtures of particles, since they show nontrivial correlations for wavevectors exceeding $\sim 2\pi/a$. For spherical particles, such correlations reflect the details of the interparticle potential and are otherwise not particularly interesting. While it may not be apparent from Figure 2, the interesting part of $S(q)$ occurs for values of q much less than $2\pi/d$ since these smaller values of q reflect the long range interparticle correlations.

2.1.2 Scattering from fractal clusters

A useful and intuitive way of characterizing the structure of many disordered materials is to specify their fractal dimension. A structure's fractal dimension is defined according to how the mass of the object scales with its radius. Trivial examples are given by: (1) a line for which $m \sim r^1$, (2) a flat sheet of paper for which $m \sim r^2$, and (3) a dense solid object for which $m \sim r^3$. In these examples of simple one, two, and three dimensional objects, $m \sim r^{d_f}$, where d_f is the dimensionality of the object. This concept can be generalized to include many structures found in nature for which $m \sim r^{d_f}$, where d_f is not an integer. A compelling example, studied extensively by light scattering, is clusters of colloidal spheres formed by irreversible aggregation when they collide while undergoing Brownian motion in a solvent. Their structure is illustrated schematically in Figure 4. From experiment and extensive computer simulation it is found that when the potential barrier to the formation of aggregates is small, such that particles almost always stick irreversibly the first time they come in contact, fractal clusters with a fractal dimension of $d_f \approx 1.7$ form. When the barrier to cluster formation is small, such particles stick irreversibly only after many close encounters and fractal clusters with a fractal dimension of $d_f \approx 2.1$ form.

To determine the scaling properties of the radial distribution function of a fractal object, recall that $n\,g(r)$ is the average density of particles a distance r from the center of the fractal aggregate. Thus, taking $m(r)$ to be the total mass within a sphere of radius

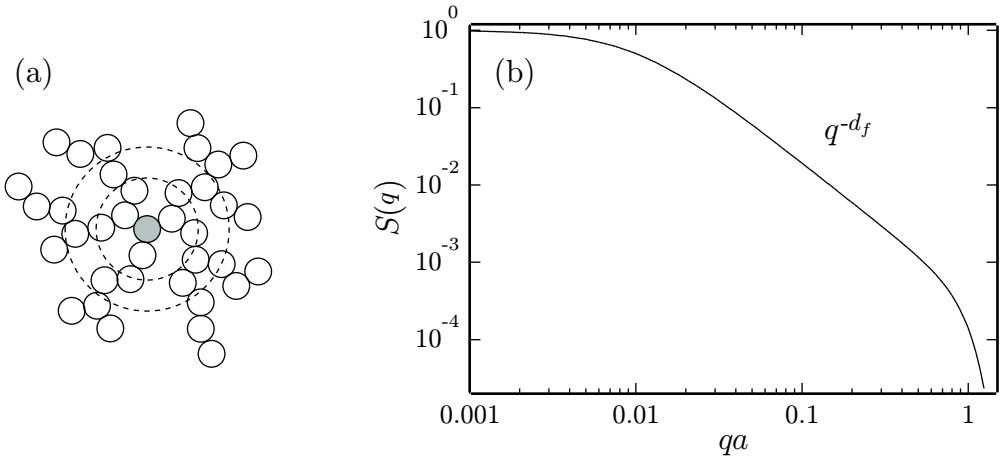

Figure 4: (a) Fractal cluster. The amount of mass m enclosed within increasingly larger spheres of radius r scales as $m \sim r^{-d_f}$ where d_f is the fractal dimension. (b) Static structure factor $S(q)$ for a fractal cluster.

r, we can write

$$\begin{aligned} n\,g(r) &= \frac{\text{mass in a spherical shell of radius } r}{\text{volume of a spherical shell of radius } r} \\ &= \frac{m(r+dr)-m(r)}{4\pi r^2\,dr} = \frac{1}{4\pi r^2}\frac{dm}{dr} \propto \frac{1}{r^2} r^{d_f-1} \,. \end{aligned}$$

Thus, we see that $g(r)$ scales with radius according to

$$g(r) \sim \frac{1}{r^{3-d_f}} \,. \tag{7}$$

When this result is substituted into Eq. (6), we find that

$$S(q) \sim q^{-d_f} \,. \tag{8}$$

This result applies to a wide variety of structures. For example, it is well known that a random walk has a fractal dimension of $d_f = 2$. Thus, for an isolated polymer chain whose conformation is well described by a random walk, it is found experimentally that $S(q) \sim q^{-2}$ over a wide range of q. Such conformations only occurs at a specific temperature T_Θ, called the theta temperature, where the net effective interactions between monomers in the chain vanishes (*i.e.* the second virial coefficient $B_2(T_\Theta)$ is zero). As the temperature is increased, the polymer coil generally expands, because of an increased favorable interaction between the monomers and the solvent, and the polymer coil expands. In this range, experiments show that $S(q) \sim q^{-5/3}$ indicating a smaller fractal dimension consistent with an expanded conformation (*i.e.* closer to a straight line). A schematic representation of $S(q)$ for an isolated polymer coil is shown in Figure 5. Note that $S(q)$ exhibits the q^{-d_f} scaling only over a finite range of q. At large q, when q is comparable to an inverse monomer diameter, the scaling behavior ceases and $S(q)$ reflects the microscopic correlations between monomers in a chain. At small q, when q is comparable to the inverse radius of gyration R_g^{-1} of the polymer chain, $S(q)$ flattens out reflecting the featureless random correlations of isolated polymer chains. Thus, on length scales greater

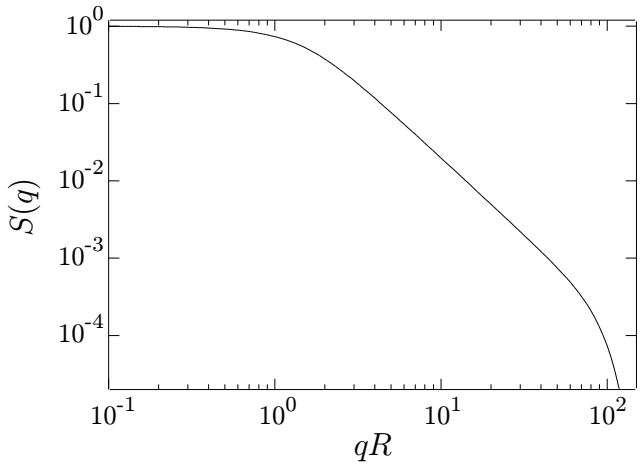

Figure 5: Structure factor for a random polymer coil.

than R_g, the isolated chains behave like an ideal gas. Although we have used the example of an isolated polymer chain, the concepts discussed here are applicable to many other systems. For example, the structure factor for a fractal aggregate exhibits similar cutoffs at small and large values of q because of the finite size of the cluster and the structure of the individual particles, respectively. Such cutoffs are observed in all physical realizations of fractal structures.

2.1.3 Scattering from density fluctuations

Up until now, we have considered the scattering of light only by particles. More generally, light is scattering by spatial fluctuations in the dielectric constant. From this point of view, the scattering of light by particles arises because the particles cause fluctuations in the dielectric constant. Indeed, if particles are suspended in a solvent with the same dielectric constant as the particles, there will be no scattering of light by the particles. In most systems, spatial fluctuations in the dielectric constant are, to within a very good approximation, equivalent to fluctuations in the particle concentration or fluctuations in the density. More importantly, useful insights into light scattering can be gained by viewing the scattering as originating from specific Fourier components of the spatial fluctuations in the density (of particles, molecules, *etc.*). In fact, it can be shown that scattering at a particular value of $\mathbf{q}$ corresponds to scattering from sinusoidal density fluctuations of the form $\exp(i\mathbf{q} \cdot \mathbf{r})$.

Consider scattering from a particular Fourier component $\exp(i\mathbf{q} \cdot \mathbf{r})$ as illustrated in Figure 6. Light is incident from the left and is scattered by sinusoidal fluctuations with wavelength $d = 2\pi/q$ in the dielectric constant. The orientation of the fluctuations is determined by the direction of the wavevector $\mathbf{q}$. The planes of constant phase are oriented at an angle $\alpha = \theta/2$ with respect the direction of the incident light. Thus, one can view the light as being reflected from the fluctuations in the dielectric constant with the angle of incidence α equal to the angle of reflection α. The scattering of light can be viewed as Bragg scattering from these sinusoidal fluctuations. In this case the Bragg

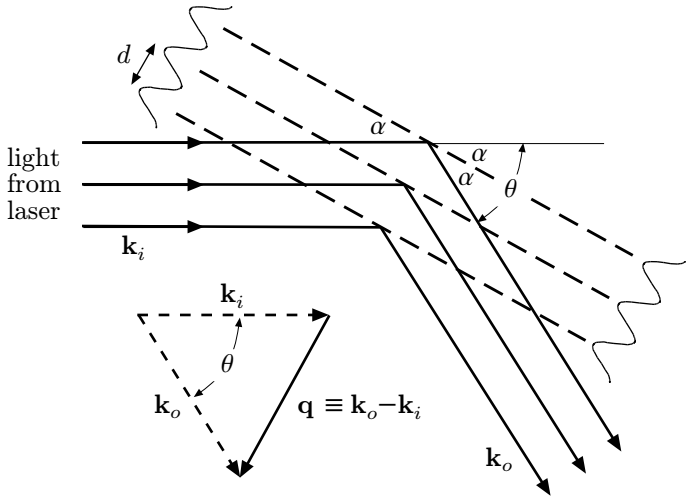

Figure 6: Scattering of light by sinusoidal density fluctuations. Light scattered at a scattering wavevector of $\mathbf{q} = \mathbf{k}_o - \mathbf{k}_i$ is scattered by sinusoidal density fluctuations $\Delta n \sim \exp(i\mathbf{q} \cdot \mathbf{r})$ with wavelength $d = 2\pi/q$.

condition can be expressed as

$$\begin{aligned} 2d \sin \alpha &= m\lambda \\ &= \lambda \,, \end{aligned} \tag{9}$$

with $m = 1$ since higher order Fourier components are absent in a *sinusoidal* fluctuation. Substituting $\alpha = \theta/2$, $d = 2\pi/q$, and $\lambda = 2\pi/q$ into Eq. (9) gives the equation $q = 2k \sin \theta/2$ which is Eq. 2. This illustrates how light scattering from the sinusoidal fluctuations in the dielectric constant is consistent with the idea that such fluctuations are equivalent to the Bragg condition for scattering. Note how this also illustrates that scattering of light at a particular wavevector $\mathbf{q}$ specifies not only the wavelength of the fluctuation that is probed by light scattering but also its spatial orientation. We are now in a position to consider how changes in the microstructure of a complex fluid caused by shear flow can be probed by light scattering.

2.1.4 The effects of shear flow on fluid structure

As a simple example of how shear flow can affect the structure of a complex fluid, we consider a droplet of oil suspended in water. In the absence of flow, the droplet will assume a spherical shape in order to minimize the interfacial energy (or surface tension) between the droplet and the water. Upon the application of a planar shear flow, $v_x = \dot{\gamma} y$, the droplet will distort. To understand how the droplet distorts, it is useful to write the shear flow as a linear superposition of pure extensional flow and pure rotation. As illustrated in Figure 7, planar shear flow can be decomposed into a linear superposition of pure extensional and pure rotational flows such that fluid elements are transformed according to $\mathbf{r}' = \mathbf{G} \cdot \mathbf{r} = (\mathbf{E} + \mathbf{\Omega}) \cdot \mathbf{r}$ where:

$$\mathbf{G} = \begin{pmatrix} 0 & \gamma & 0 \\ 0 & 0 & 0 \\ 0 & 0 & 0 \end{pmatrix} \tag{10}$$

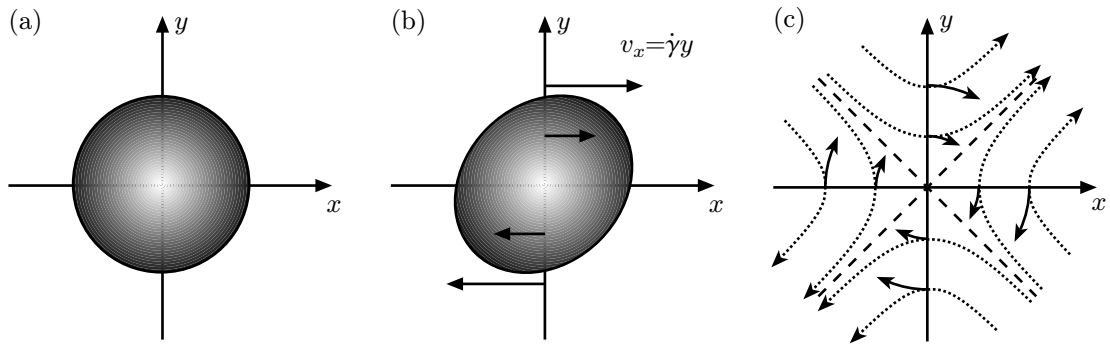

Figure 7: Effect of shear flow on the shape of a droplet. (a) A spherical droplet (b) is deformed by shear flow. (c) Planar shear flow can be decomposed into a linear superposition of pure extensional (dotted lines) and pure rotational flows (solid lines).

and

$$\mathbf{E} = \begin{pmatrix} 0 & \gamma/2 & 0 \\ \gamma/2 & 0 & 0 \\ 0 & 0 & 0 \end{pmatrix} , \; \mathbf{\Omega} = \begin{pmatrix} \cos\omega t & \sin\omega t & 0 \\ -\sin\omega t & \cos\omega t & 0 \\ 0 & 0 & 1 \end{pmatrix} , \tag{11}$$

where γ is the strain and the rotation frequency ω is half the strain rate $\dot{\gamma}$. The shear strain γ is related to the shear rate (or strain rate) $\dot{\gamma} = v_x/y$ by the equation $\gamma = \dot{\gamma}t$. The effect of the extensional flow is to distort the droplet along a line oriented 45° to the x-axis while the effect of the rotational flow is merely to distort the droplet. To understand the effect of flow on a concentration fluctuation, consider the following thought experiment. Imagine that a spherical fluctuation instantaneously comes into existence in a shear flow at time $t = 0$. The initial effect of the shear flow will be to stretch the droplet along a line oriented 45° to the x-axis and then to rotate it slightly towards the x-axis. How far the droplet is ultimately stretched and rotated depends on the relaxation rate Γ or lifetime $\tau \equiv 1/\Gamma$ of the fluctuation compared to the shear rate $\dot{\gamma}$. If $\Gamma \gg \dot{\gamma}$, then the fluctuation will be stretched only slightly and hardly rotated at all away from 45° before it disappears. If $\Gamma \ll \dot{\gamma}$, then the fluctuation can be stretched much more and can be rotated until it is essentially aligned with the x-axis. Of course, the degree to which the droplet is stretched also depends on the surface tension of the droplet, its radius, and on the relative viscosities of the fluid inside and outside the fluctuation. If the fluctuation in concentration is not very large, as is typically the case, then the droplet can be expected to deform affinely with the macroscopic applied shear flow field. In any case, the degree to which the droplet is rotated depends primarily on the whether its lifetime τ is short or long compared to the time it takes for the droplet to be distorted and rotated towards the x-axis. The two limiting cases, in which $\Gamma \gg \dot{\gamma}$ and $\Gamma \ll \dot{\gamma}$ are illustrated in Figure 8(a) and (b).

It is also useful to consider how light is scattered from such fluctuations and what the resulting scattering patterns would be. Thus, we imagine that we perform a light scattering experiment on the fluctuations illustrated in Figure 8. We arrange the experiment so that the scattering wavevector $\mathbf{q}$ always lies in the x-y plane. Following our discussion in Section 2.1.1, we expect that the scattering patterns will be related to the Fourier transforms of the real-space distribution of matter. In Figure 8(c) and (d), we illustrate schematically the basic symmetries of the scattering patterns that would result

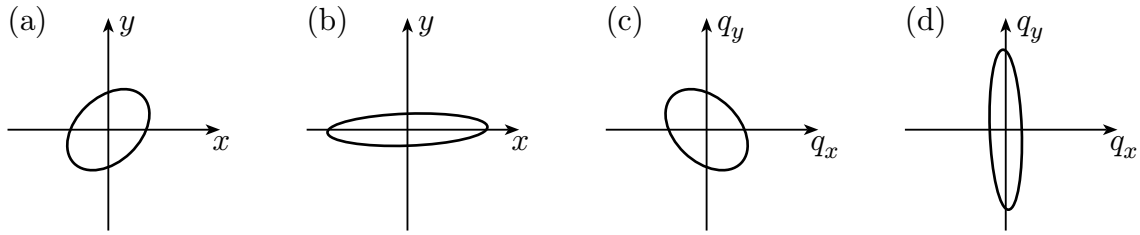

Figure 8: Effect of shear flow on the shape of fluctuations and the resulting scattering patterns. (a) A fluctuation where $\Gamma \gg \dot{\gamma}$ (b) A fluctuation where $\Gamma \ll \dot{\gamma}$. (c) Scattering pattern corresponding to (a). (d) Scattering pattern corresponding to (b).

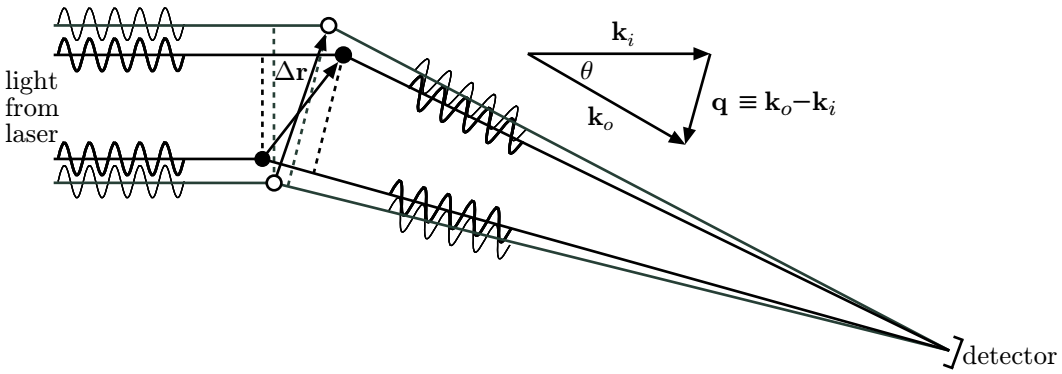

Figure 9: Schematic for dynamic light scattering of two light paths from two particles. The filled and open circles indicate the positions of the two particles at times t and $t + \tau$, respectively.

from scattering from the fluctuations shown in Figure 8(a) and (b). One can view the scattering as being qualitatively similar to what one would obtain from diffraction from a slit oriented in the same fashion as the concentration fluctuation. Thus, the narrow parts of the fluctuations result in scattering over a broad range of angles and the wide parts of the fluctuations results in scattering over a narrow range of angles (or equivalently, a broad or narrow range of q vectors – recall Eq. (2).

2.2 Dynamic light scattering

Dynamic light scattering (DLS), as its name suggests, probes the temporal evolution of the concentration fluctuations measured in static light scattering. To understand the basic ideas behind dynamic light scattering we once again consider scattering from two particles as illustrated in Figure 9. As in the case of static scattering, the relative phases at the detector of the light scattered from the two particles determines the degree to which there is constructive or destructive interference. As the particles move, the differences in the path lengths $\Delta\mathbf{r}$ between the pair of particles changes causing their relative phases at the detector to change. Thus, as the particles move, the intensity of light at the detector fluctuates in time. The typical time scale for the duration of a fluctuation is determined by the time it takes the relative phase differences between the two paths to change by approximately unity. This means that $\Delta\mathbf{r}(t+\tau) - \Delta\mathbf{r}(t) \sim \lambda/\sin(\theta/2)$. If we assume that each particle moves randomly and independently of every other particle, then to within a

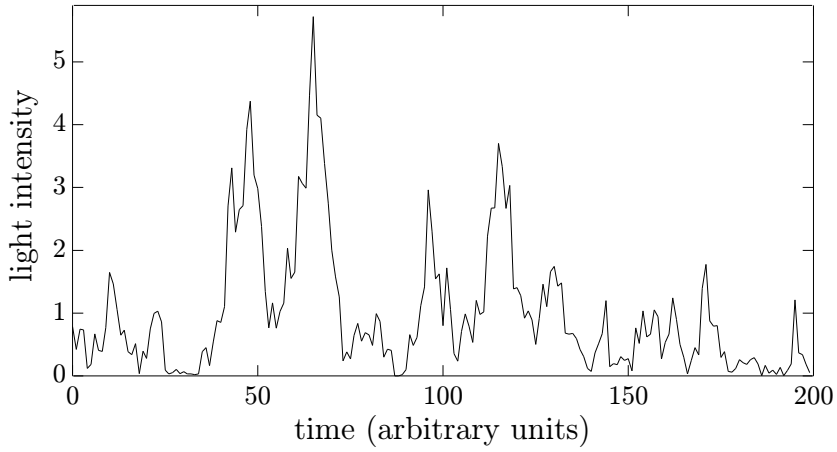

Figure 10: Intensity *vs.* time for light scattering from a suspension of 2000 diffusion particles. The average intensity of this plot is unity and the characteristic time of the fluctuations in approximately 15 time units.

factor of order unity this condition can be expressed more simply in terms of the motion of a single particle as $\mathbf{r}(t+\tau) - \mathbf{r}(t) \sim \lambda/\sin(\theta/2)$. Thus, the lifetime of a fluctuation is determined by the time it takes particles to move approximately the wavelength of light, or somewhat farther depending on the scattering angle θ.

We can generalize this analysis to a collection of N scatterers. In that case the electric field at the detector can be written as

$$\mathbf{E}_d(t) = \mathbf{E}_s \sum_{i=1}^{N} e^{i\mathbf{q}\cdot\mathbf{r}_i(t)} \ , \tag{12}$$

where for simplicity we take the scattering amplitude to be the same for all scatterers as would be the case for a collection of identical spherical particles. The intensity of the scattered light is proportional to the square modulus of the electric field at the detector, *i.e.*

$$I(t) \propto |\mathbf{E}_d|^2 = |\mathbf{E}_s|^2 \sum_{i,j}^{N} e^{i\mathbf{q}\cdot[\mathbf{r}_i(t)-\mathbf{r}_j(t)]} \ . \tag{13}$$

From this result we see that for N scatterers the scattered intensity is determined by the differences in phases between pairs of light paths, just as for the case of a pair of particles discussed above. Since the scattering volume (*i.e.* the volume of sample from which scattered light is collected) is typically much larger than spatial extent of fluctuations, the sum in Eq. (12) represents a sum over many independent fluctuations. Thus, the electric field $E_d(t)$ in Eq. (12) is the sum of many independent random variables and, according to the Central Limit Theorem, is a random Gaussian variable. Since $I(t) \propto |\mathbf{E}_d|^2$,this means that the intensity of scattered light is distributed according to $P(I) = \exp(-I/\langle I\rangle)/\langle I\rangle$. In Figure 10, we plot the intensity of the scattered light as a function of time obtained from Eq. (13) for 2000 randomly diffusing particles. It is interesting and important to note that the fluctuations do not diminish as the number of particles increases; in fact, the amplitude of the intensity fluctuations actually increases. It is this feature of scattered light that makes dynamic light scattering feasible, since there are on the order of 10^{12} or more scatterers in a typical scattering experiment. As stated previously, the duration of

a typical fluctuation is given by the time it takes for the phase of the light scattered from a particle to change by order unity, *i.e.* $\mathbf{q} \cdot [\mathbf{r}(t+\tau) - \mathbf{r}(t)] \equiv \mathbf{q} \cdot \Delta\mathbf{r}(\tau) \sim 1$.

The temporal evolution of the intensity fluctuations of the scattering light reflect the stochastic motion of the scatterers. For example, if we heat the sample so that the scatterers move more rapidly, the intensity of the scattered light will fluctuate more rapidly. In order to extract this information, we need some quantitative means for characterizing the statistics of the temporal fluctuations of the scattered light. This is most frequently accomplished by calculating the temporal autocorrelation function $g_I(t,\tau)$ of the scattered light:

$$g_I(t,\tau) \equiv \frac{\langle I(t+\tau)I(t)\rangle}{\langle I(t)\rangle^2} \ , \tag{14}$$

where the brackets indicate a temporal average taken over the duration of the experiment. Alternatively, it is often convenient to introduce the temporal autocorrelation function of the scattered electric field $g_E(t,\tau)$ defined as

$$g_E(t,\tau) \equiv \frac{\langle E(t+\tau)E(t)\rangle}{\langle I(t)\rangle} \ . \tag{15}$$

For scattered fields with Gaussian statistics, these two correlation functions are related by the Siegert relation [1],

$$g_I(t,\tau) = 1 + |g_E(t,\tau)|^2 \ . \tag{16}$$

To obtain a statistically meaningful sampling of the temporal fluctuations, an experiment should ideally aquire data over a time scale which is long compared to the time scale of the longest relaxation time of the system. If the system is stationary, that is, if its dynamics do not change with the passage of time, then $g_I(t,\tau)$ will be independent of t and will depend only on τ. In this case, we can write $g_I(t,\tau) = g_I(\tau)$. For $\tau \to 0$, $g_I(\tau) \to \langle I^2(t)\rangle / \langle I(t)\rangle^2 = 2$, where the last equality follows for the typical case where the scattered electric field obeys Gaussian statistics (as discussed above). For τ much greater than the duration of the longest lived fluctuation of the system τ_M, the scattered intensity at time $t+\tau$ becomes independent of the scattered intensity at time t, and $\langle I(t+\tau)I(t)\rangle$ factorizes into $\langle I(t+\tau)\rangle\langle I(t)\rangle = \langle I(t)\rangle^2$. Thus, for $\tau \to \infty$, $g_I(\tau) \to 1$.

Therefore, we expect that the correlation function $g_I(t,\tau)$ will in general decay from a value of 2 for $\tau = 0$ to unity for $\tau \gg \tau_M$ or, equivalently, that $g_E(t,\tau)$ will decay from unity for $\tau = 0$ to zero for $\tau \gg \tau_M$. The time over which these correlation functions decay and the functional form of the decay will depend on the dynamics of the system. As an example, we consider a system whose dynamics are governed by simple diffusion. In this case, we imagine that fluctuations in the concentration of particles (scatterers) given by $\delta c(\mathbf{r},t) \equiv c(\mathbf{r},t) - \langle c\rangle$ is governed by the diffusion equation

$$\frac{\partial}{\partial t}\delta c(\mathbf{r},t) = D\nabla^2 \delta c(\mathbf{r},t) \ , \tag{17}$$

where D is the diffusion coefficient of the concentration fluctuations. Because light is scattered by sinusoidal fluctuations in the concentration of scatterers, it is useful to consider the spatial Fourier transform of Eq. (17):

$$\frac{\partial}{\partial t}\delta c(\mathbf{q},t) = -Dq^2 \delta c(\mathbf{q},t) \ , \tag{18}$$

where

$$\delta c(\mathbf{q},t) = \int_V \delta c(\mathbf{r},t)\, e^{i\mathbf{q}\cdot\mathbf{r}}\, d\mathbf{r}\ . \tag{19}$$

Solving Eq. (18) for $\delta c(\mathbf{q},t)$, we find

$$\delta c(\mathbf{q},t) = \delta c(\mathbf{r},0)\, e^{-Dq^2 t}\ . \tag{20}$$

Thus, we find that spatial fluctuations in the concentration with a wavelength of $2\pi/\lambda$ relax with a time constant of $1/Dq^2$. The temporal autocorrelation functions for scattered light reflect these dynamics.

Starting from Eqs. (12) and (15) and writing the phase of the scattered light as $\phi(t) \equiv \mathbf{q}\cdot\mathbf{r}_i(t)$, we can calculate $g_E(\tau)$ and, via the Siegert relation given by Eq. (16), $g_I(\tau)$:

$$\begin{aligned} g_E(\tau) &= \frac{1}{n}\left\langle \sum_{i,j}^{N} e^{i\mathbf{q}\cdot[\mathbf{r}_i(t+\tau)-\mathbf{r}_j(t)]} \right\rangle && (21)\\ &= \frac{1}{n}\left\langle \sum_{i}^{N} e^{i\mathbf{q}\cdot[\mathbf{r}_i(t+\tau)-\mathbf{r}_i(t)]} \right\rangle && (22)\\ &= \frac{1}{n}\left\langle \sum_{i}^{N} e^{i\Delta\phi_i(\tau)} \right\rangle\ , && (23) \end{aligned}$$

where we define the change in phase for a scattering from a single particle as $\Delta\phi_i(\tau) \equiv \mathbf{q}\cdot[\mathbf{r}_i(t+\tau)-\mathbf{r}_i(t)]$. In passing from Eq. (21) to Eq. (22), we have assumed that interactions between particles are not important so we can ignore terms in the sum where $i \neq j$. The sum in Eq. (23) is a sum over light paths through the sample where each path involves exactly one scattering event from a particle and at a wavevector $\mathbf{q}$. Thus, if all the particles are identical, then all the paths are statistically equivalent and we can simplify Eq. (22) by writing it as the ensemble average over a single path:

$$\begin{aligned} g_E(\tau) &= \left\langle e^{i\Delta\phi(\tau)} \right\rangle && (24)\\ &= e^{-\frac{1}{2}\langle\Delta\phi^2(\tau)\rangle}\ , && (25) \end{aligned}$$

Equation (25) follows from Eq. (24) if, as is usually the case, the distribution of phase differences $\Delta\phi$ is Gaussian. Since $\Delta\phi(\tau) = \mathbf{q}\cdot\mathbf{r}$

$$\langle\Delta\phi^2(\tau)\rangle = \frac{1}{3}q^2\langle\Delta r^2(\tau)\rangle\ , \tag{26}$$

where the factor of $1/3$ comes from performing the 3-d angular average $\langle\cos^2\theta\rangle_{\theta,\phi}$ over the unit sphere. For simple particle diffusion, the mean square displacement is given by $\langle\Delta r^2(\tau)\rangle = 6D\tau$ which leads to the result:

$$g_E(\mathbf{q},\tau) = e^{-\frac{1}{6}q^2\langle\Delta r^2(\tau)\rangle} = e^{-Dq^2\tau}\ . \tag{27}$$

or equivalently

$$g_I(\mathbf{q},\tau) = 1 + e^{-2Dq^2\tau}\ . \tag{28}$$

Note the similarity of these results to Eq. (20). For interacting particles, similar results are often obtained with the additional modification that the diffusion coefficient D becomes q-dependent. Thus, fluctuations of different wavelengths relax with a q-dependent relaxation rate of $q^2D(q)$.

2.2.1 Dynamic light scattering in steady shear flow

In these lectures, we are particularly interested in examining the dynamics of systems driven away from equilibrium by the application of shear flow. Thus, it is natural to ask what happens to $g_I(t,\tau)$ for a system subjected to shear. To simplify the discussion, we first consider the case where the scatterers are randomly distributed throughout the sample and move only in response to an imposed shear flow (*e.g.* there is no Brownian motion). The detailed analysis of dynamic scattering from a system undergoing shear is complex. But the basic ideas can be understood by noting that dynamic light scattering is sensitive to *differences* in particle velocities. This is easily appreciated by studying Figure 9 from which it is evident that the relative phases of light scattered from different particles does not change if all the particles move with the same uniform motion. In a homogeneous shear flow, however, particles move with different velocities depending upon their relative positions within the scattering volume. The particles the farthest apart along the velocity gradient and within the scattering volume have the greatest velocity difference $\Delta\mathbf{v}$. This can be written as $\Delta\mathbf{v} = \dot{\gamma}\mathbf{d}$, where $\mathbf{d}$ is the distance across the scattering volume in the direction of the velocity gradient. Thus, to within numerical factors of order unity, the characteristic decay time τ_S of $g_E(\tau)$ for a sheared system is $1/\mathbf{q}\cdot\Delta\mathbf{v} = (\dot{\gamma}\mathbf{q}\cdot\mathbf{d})^{-1}$. To within the same level of approximation, the decay of the correlation function is given by $g_E(\tau) \sim \exp[-(\mathbf{q}\cdot\mathbf{d}\dot{\gamma}\tau)^2]$ Note that for homogeneous shear flow, the correlation function decays with a Gaussian time dependence rather than the simple exponential time dependence found for diffusion. This result simply reflects the fact that in a shear flow, the separation between pairs of particles grows linearly in time whereas for diffusion, the separation between particles grows as the square root of time.

We now consider what happens when there is Brownian motion. For shear rates much smaller than the slowest relaxation rate τ_M^{-1}, that is for $\dot{\gamma}\tau_M \ll 1$, the internal dynamics of the system relax on time scales much faster than the rate at which shear can alter the structure of the system. In this case, the Brownian motion is unaffected by the presence of the shear flow. The more interesting situation is the case where the shear rate is sufficiently high to alter the structure of the system before it can relax by it usual equilibrium dynamics, that is, when $\dot{\gamma}\tau_M \gg 1$. In this case, there will be two contributions to the decay of $g_E(\tau)$: the decay resulting from the shear flow itself (discussed in the previous paragraph) and the decay resulting from the Brownian motion (possibly modified by the presence of the shear flow). The ratio of the characteristic decay times for these processes is given by

$$\frac{\tau_M}{\tau_S} = \frac{\tau_M}{(\dot{\gamma}\mathbf{q}\cdot\mathbf{d})^{-1}} = \dot{\gamma}\tau_M\mathbf{q}\cdot\mathbf{d}\,. \tag{29}$$

Scattering volumes for sheared systems are typically no smaller than 50 μm. Taking $d \sim 50$ μm and $q \sim 10^5$ cm^{-1}, $\mathbf{q}\cdot\mathbf{d} \sim 50$. Thus, in the physically interesting case when $\dot{\gamma}\tau_M \sim 1$, the time scale for the decay of $g_E(\tau)$ from the shear motion τ_S can be expected to be approximately 50 times faster than the time scale τ_M decay due to the intrinsic dynamics of the system. Thus, the physically interesting change in the system dynamics due to shear flow is masked by the effect of the shear flow itself on the decay of $g_E(\tau)$. In principle, this problem can be circumvented by making $\mathbf{q}$ perpendicular to $\mathbf{d}$. In practice, however, this is very difficult to achieve. Moreover, it limits measurement of the change in the system dynamics only to those fluctuations which are in the direction perpendicular to the velocity gradient. Therefore, one must seek other methods for measuring the change

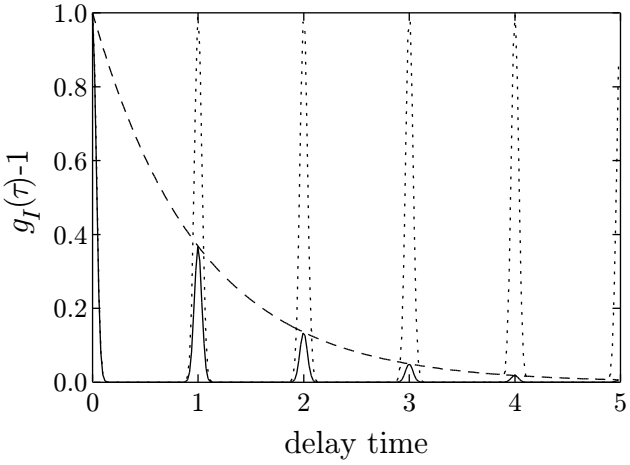

Figure 11: Appearance of echoes in the intensity autocorrelation function for oscillatory shear flow. In the absence of irreversible motion of the scatterers, the echoes are unattenuated (dotted line). When there is irreversible motion, the echoes are attenuated (solid line). The envelope of the echo heights (dashed line) is determined by the amount of irreversible motion.

in the system dynamics arising from the application of shear flow. Such methods have been developed and are discussed in the next section.

2.2.2 Dynamic light scattering in oscillatory shear flow

To develop a method to measure the dynamics of a system under shear flow, we exploit the fact that shear flow is deterministic and reversible, while Brownian motion is not. First, we consider light scattering from a system undergoing oscillatory shear flow where, as in the previous section, there is no Brownian motion. Suppose our system consists of randomly distributed non-Brownian spheres suspended in a liquid undergoing sinusoidal planar shear flow with a period $T \ll \tau_S$. For decay times such that $\tau_S < \tau < T$ we can ignore the fact that the shear flow is oscillatory. In this case, $g_E(\tau)$ decays on a time scale $\tau_S \sim (\dot{\gamma}\mathbf{q}\cdot\mathbf{d})^{-1}$ in the same way as it would for steady shear flow (here, $\dot{\gamma}$ should be taken to be some characteristic shear such as the rms shear rate).

Upon the reversal of the flow field, however, the situation becomes qualitatively different from that of steady shear flow; the suspended particles retrace their trajectories so that they return to their same exact positions every period T. Therefore, the scattered light will always be perfectly correlated with itself an integral number of periods T ago. Thus, the temporal autocorrelation function will consist of a series of echoes spaced one period apart. The height of the echoes will be unity as long as the particles return to precisely the same position they were at one period ago. The width of the echoes will be twice the width of the initial decay arising from the shearing motion. A correlation function corresponding to this situation is illustrated in Figure 11 by the dotted lines.

With the addition of Brownian motion, there is irreversible movement of the scatterers between echoes and the echoes do not return to their full height. The attenuation of the echos is a quantitative measure of the irreversible motion and is determined by the nonequilibrium dynamics of the system, as illustrated in Figure 11. In the simplest case,

when $\dot{\gamma}\tau_S < \dot{\gamma}\tau_M \ll 1$, the envelope which determines the attenuation of the echoes is exponential and simply given by the equilibrium decay $g_I(\tau) = 1 + \exp(-2Dq^2\tau)$. The physically interesting case occurs when $\dot{\gamma}\tau_M$ becomes comparable to or exceeds unity. In this case, one generally expects the dynamics of the system to depart from their equilibrium behavior; normally, relaxation rates increase as the shear provides more efficient paths for fluctuations to relax as compared to the equilibrium case. We will provide examples of how such measurements can be used to probe glassy emulsions in Section 4.

2.2.3 Diffusing-wave spectroscopy

Many complex fluids and fragile materials consist of structures with characteristic length scales comparable to or larger than the wavelength of light. Examples of such systems include colloidal suspensions, emulsions, and foams which are typically made up of micron-sized solid, liquid, or gas particles, respectively, in a liquid matrix. The presence of such structures leads to spatial fluctuations in the refractive index (or dielectric constant) on a length scale comparable to light. As a result, there is multiple scattering of light such that all but the thinnest samples of such materials are opaque. If such a material does not absorb light significantly, these materials appear white (this is typically the case). Thus, normal light scattering which requires that the light be scattered no more than once is not feasible.

Presently, there are two methods that have proven useful for extracting quantitative information from light scattering on systems which multiply scatter light. The first is a dynamic light scattering technique which uses two lasers with different wavelengths. The lasers and optics are aligned in very clever way so as to discriminate against multiply scattered light. In this scheme, only singly scattered light contributes significantly to the dynamical signal even though there may be significant multiple scattering. The technique is difficult to set up and costly to instrument. Nevertheless, it is a powerful tool provided there is sufficient singly scattered light to provide a measurable signal.

The second approach, called diffusing-wave spectroscopy (DWS)[2], is completely different. Instead of discriminating against multiply scattered light, one exploits it. The primary task is to describe the transport of light sufficiently well so quantitative information can be extracted from a measurement. Fortunately, and perhaps surprisingly, such an enterprise is not difficult. In fact, the experiments are exceedingly simple to instrument – even simpler and less costly than conventional single scattering experiments.

The determination of the electromagnetic fields inside a sample which exhibits a high degree of multiple scattering is a complex task. Fortunately, it is not necessary to specify the electromagnetic field everywhere within the sample in order to extract useful information about the sample from the multiply scattered light. Instead, it is sufficient to consider a single pair of light paths through the sample, in much the same way as we did for singly scattered light in Figure 9. Consider two light paths consisting of light scattered many times by different particles while passing through a sample as illustrated in Figure 12. The time of flight for the light through the sample is essentially instantaneous since it occurs on a time scale of 100 ps or less, which is much less than any time scale we will be interested in for the motion of the particles. Nevertheless, light emerging from the sample after having scattered many times will have a phase that depends on the precise optical path length through the sample. The intensity of the scattered light at the detector will

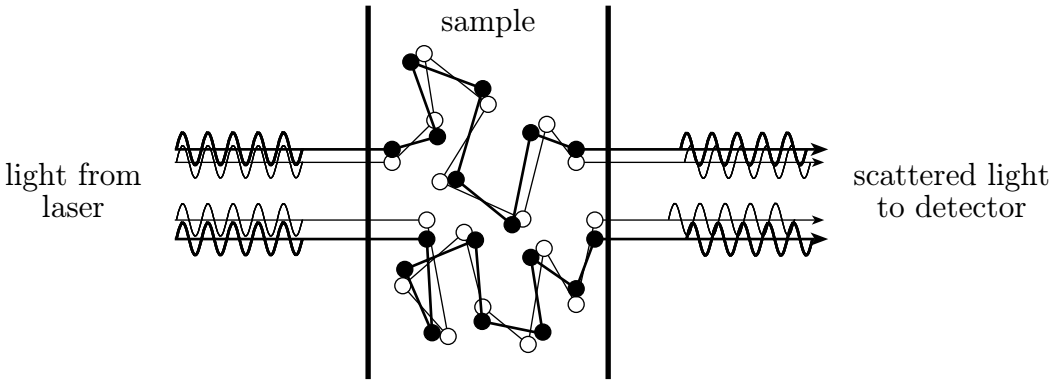

Figure 12: Schematic for multiple dynamic light scattering of two light paths from many particles. The filled and open circles indicate the positions of the particles for the two paths at times t and $t + \tau$, respectively. Particles not involved in the scattering of the two represented light paths are present but not shown for clarity.

depend on the exact relationship between all these phases of the light coming from different paths through the sample. As the particles within the sample move, the path lengths for the light through the sample change. This, in turn, changes the phase relationships between the different pairs of light paths incident on the detector and causes the light intensity to fluctuate, just as in the case of single scattering DLS.

As for DLS, we seek to characterize the fluctuations in the scattered light arising from the motion of particles by calculating the correlation function $g_E(\tau)$ (recall that we can obtain $g_I(\tau)$ using the Siegert relation given by Eq. (16)). The calculation proceeds similarly to our calculation in the single scattering case. In fact, we write $g_E(\tau)$ just as we did before starting with the sum over scattering paths represented in Eq. (23):

$$g_E(\tau) = \frac{1}{N_p} \left\langle \sum_i^{N_p} e^{i\Delta\phi_i(\tau)} \right\rangle \ , \tag{30}$$

where we emphasize that here, as in the single scattering case, the sum is over the number of light scattering *paths* N_p through the sample. In contrast to the situation for single scattering, however, here each path consists of many scattering events, as depicted in Figure 12. Moreover, different scattering events within a path occur at different wavevectors whereas for the case of single scattering, each path involved scattering from a single particle and at a single wavevector which was the same for all paths.

Let us denote the number of scattering events in the i^{th} path as n_i. Then, the phase difference $\Delta\phi_i(\tau)$ for a given path in Eq. (30) involves a sum over all the n_i scattering events for that path. That is,

$$\Delta\phi_i(\tau) = \sum_{j=1}^{n_i} \mathbf{q}_j \cdot \mathbf{r}_j(t+\tau) - \sum_{j=1}^{n_i} \mathbf{q}_j \cdot \mathbf{r}_j(t)] = \sum_{j=1}^{n_i} \mathbf{q}_j \cdot \Delta\mathbf{r}(\tau) \ . \tag{31}$$

where $\Delta\mathbf{r} = \mathbf{r}_j(t+\tau) - \mathbf{r}_j(t)$. In the case of multiple scattering, paths may have any number of scattering events but only those paths with the same number of scattering events can be regarded as statistically equivalent. Thus, the analysis of multiple light scattering is somewhat more complicated than for the case of single scattering.

The first step in the analysis of Eq. (30) is to consider only paths with a given number of scattering events $n = n_i$ (dropping the now superfluous subscript). Next, we note that the statistical distribution of phases $\Delta\phi_n$ for paths of a given length n is Gaussian. In the case of multiple scattering, this is an even better approximation than for the case of single scattering because here the phase is the sum of many random variables; by the Central Limit Theorem, such a sum should obey Gaussian statistics (in the limit of large n). The contribution to the total correlation function $g_E(\tau)$ for all the paths having a given number of scattering events n is:

$$\begin{aligned} g_E^n(\tau) &= \frac{N_n}{N_p}\left\langle e^{i\Delta\phi_n(\tau)}\right\rangle \\ &= \frac{N_n}{N_p} e^{-\frac{1}{2}\langle\Delta\phi_n^2(\tau)\rangle} , \end{aligned} \tag{32}$$

where N_n/N_p is the fraction of paths with exactly n scattering events. The mean square phase difference for paths with n steps is obtained by squaring and averaging over Eq. (31)

$$\langle\Delta\phi_n^2(\tau)\rangle = \sum_{j=1}^{n}\left\langle[\mathbf{q}_j\cdot\Delta\mathbf{r}_j(\tau)]^2\right\rangle \tag{33}$$

$$= n\frac{1}{3}\langle q^2\rangle\langle\Delta r^2(\tau)\rangle , \tag{34}$$

where we have made the assumption that only the diagonal terms in the squared sum are non-zero, consistent with our assumption that the position and motion of different particles are independent. The averages over q^2 and $\Delta r(\tau)^2$ factorize because the scattering wavevectors are independent of the particle motion.

To obtain the full correlation function for light paths of all orders, we sum Eq. (32) over all path lengths:

$$g_E(\tau) = \sum_n^{\infty}\frac{N_n}{N_p}e^{-\frac{1}{2}\langle\Delta\phi_n^2(\tau)\rangle} \tag{35}$$

$$= \sum_n^{\infty}\frac{N_n}{N_p}e^{-n\langle q^2\rangle\langle\Delta r(\tau)^2\rangle/6} . \tag{36}$$

Note that in passing from Eq. (30) to Eq. (36) we have changed the sum from a sum over all paths to a sum over all *path lengths* with each path length weighted by the fraction of paths N_n/N_p with a given number of scattering events n.

The sum in Eq. (36) cannot in general be performed analytically. Therefore, we approximate the sum over the number of scattering events n in a path by passing to the continuum limit and performing an integral over the length of a path $s = nl$, where l is the mean free path between scattering events. The fraction N_n/N_p of paths consisting of n scattering events becomes the fraction (or probability) $P(s)$ of paths of length s. The mean square phase difference undergoes the following transformation:

$$\frac{1}{2}\langle\Delta\phi_n^2(\tau)\rangle = n\langle q^2\rangle\langle\Delta r^2(\tau)\rangle/6 \tag{37}$$

$$= \frac{s}{l}\,2k^2\langle 1-\cos\theta\rangle\,\langle\Delta r^2(\tau)\rangle/6 \tag{38}$$

$$= \frac{s}{3l^\star}k^2\langle\Delta r^2(\tau)\rangle , \tag{39}$$

where we have used the fact that $\langle q^2 \rangle = 2k^2 \langle 1 - \cos\theta \rangle$ and that the transport mean free path is given by $l^\star \equiv l/\langle 1 - \cos\theta \rangle$. Here θ is the scattering angle and $k \equiv 2\pi/\lambda$. From the definition of $l^\star$ it is clear that $l^\star \geq l$. Physically, $l^\star$ is the length scale over which the direction of scattered light is randomized (*i.e.* the characteristic length scale over which scattered light loses memory of its initial direction of propagation). Since scatterers comparable to or larger than the wavelength of light tend to scatter preferentially in the forward direction, several scattering events may be required to randomize the direction of light propagation. In this case, $l^\star > l$. For small particles where the scattering is essentially isotropic, $l^\star \simeq l$.

Using these results, we can convert the sum in Eq. (36) to an integral over path lengths:

$$g_E(\tau) = \int_0^\infty P(s)\, e^{-k^2 \langle \Delta r^2(\tau) \rangle s/(3l^\star)}\, ds \; . \tag{40}$$

For diffusing particles where $\langle \Delta r^2(\tau) \rangle = 6D\tau$, Eq. (40) can be rewritten as

$$g_E(\tau) = \int_0^\infty P(s)\, e^{-2Dk^2 \tau s/l^\star}\, ds \; . \tag{41}$$

To evaluate Eq. (41), one must determine the distribution of path lengths $P(s)$. For samples which exhibit a high degree of multiple scattering, the path the light takes in traversing the sample can be described as a random walk. Typically, the transport occurs over a length scale much greater than the mean free path $l^\star$ (typically $l^\star \sim 10^2$ μm and sample dimensions $\sim 10^3$ μm). In this limit, where the characteristic dimension traversed by random walk is much larger than the basic step length, the random walk can be described by diffusion. Using these ideas, Eqs. (40) and (41) can be solved for a variety of situations.

Consider, for example, a sample confined between two parallel glass plates a distance L apart with light from a laser incident on one side. If one detects scattered light emerging from the opposite side of the samples, then one obtains [2]

$$g_E(\tau) \simeq \frac{x}{\sinh x} \tag{42}$$

where

$$x = \frac{L}{l^\star} \sqrt{k^2 \langle \Delta r^2(\tau) \rangle} \; . \tag{43}$$

For the case of particles (scatterers) which diffuse with a diffusion coefficient D,

$$x = \frac{L}{l^\star} \sqrt{6Dk^2 \tau} \; . \tag{44}$$

In this case, the decay of the correlation function is approximately exponential with characteristic decay time of $(l^\star/L)^2/Dk^2$. For single scattering, the characteristic decay time is $1/Dq^2 \sim 1/Dk^2$. Thus, the decay of the correlation function for multiple scattering is faster than the decay for single scattering by a factor of approximately $(L/l^\star)^2$. Physically, this acceleration of the decay is easy to understand. For both single and multiple scattering, the correlation function decays in the time that it takes the phase $\Delta\phi(\tau)$ of the scattered light to change by approximately 1. For the case of single scattering this means that a particle must move by a distance $\sim 1/q \sim \lambda$ or roughly the wavelength of light. For the case of multiple scattering, each particle in a given path must move only

λ/n, where n is the number of scattering events in a typical light path in order for the entire path length to change by approximately the wavelength of light. This is reflected in Eqs. (26) and (34) for the mean square phase change for single and multiple light scattering, respectively; Eq. (34) has a factor of n which is not present in from Eq. (26). Since the end-to-end distance for a random walk scales as the square root of the number of steps, the decay of $g_E(\tau)$ is a factor of $(L/l^\star)^2$ faster for multiple scattering than for single scattering.

Thus, perhaps the single most important difference between single and multiple dynamic light scattering is the fact that multiple dynamic light scattering, or DWS, is much more sensitive to very small particle motions. For a typical DWS transmission experiment where $(L/l^\star) \sim 10$, the characteristic distance a typical particle moves in a decay time decay is $\lambda/n \sim \lambda/(L/l^\star)^2 \sim \lambda/100$ or about 50 Å. With some effort and care, rms particle motions on much smaller scales can be resolved with the current record being somewhat less than 1 Å. We will return to our discussion of DWS in Section 4 where we illustrate the use and sensitivity of DWS in a study of the response of disordered emulsions to oscillatory shearing motion. In the next section, we present the results of some experiments on shear thickening which demonstrates, among other things, how single light scattering can be used to study complex fluids and fragile materials.

3 Shear thickening in wormlike micellar solutions

Solutions of wormlike micelles exhibit a fascinating range of rheological behavior. Above the overlap concentration, their linear rheological behavior is deceptively simple. A fairly complete theoretical description based on a modified reptation picture is available and has been remarkably successful in describing a wide variety of experiments [3]. In this section, however, we are concerned with another class of wormlike micellar systems, micellar solutions near and below the overlap concentration which exhibit nonlinear shear thickening. The shear-thickening behavior is quite dramatic and continues to puzzle researchers after more than 15 years of intensive research [4, 5]. Before reviewing the behavior of these systems, we briefly review some basic ideas concerning wormlike micellar solutions.

3.1 Basic properties of shear-thickening micellar solutions

Surfactants are molecules with a dual personality: one part of the molecule is hydrophillic or water-loving and the other part is hydrophobic or water-hating. They are useful in a variety of contexts, most notably perhaps in promoting the mixing of chemically incompatible liquids by reducing the interfacial tension between the two liquids. Our interests, however, lie elsewhere. The surfactants we are interested in consist of molecules with fairly compact hydrophillic ionic polar head groups and hydrophobic hydrocarbon tails which typically have about 16 carbon molecules. Below a certain concentration called the *critical micelle concentration* or *cmc*, the surfactants exist as single molecules in aqueous solution; the cmc is typically on the order of 1 mM but can be significantly lower or higher. Above the cmc, these molecules form small aggregates, typically spherical just above the cmc, but often taking on other shapes as the concentration is increased.

Aggregates of surfactants form in order to hide their hydrophobic tails from the sur-

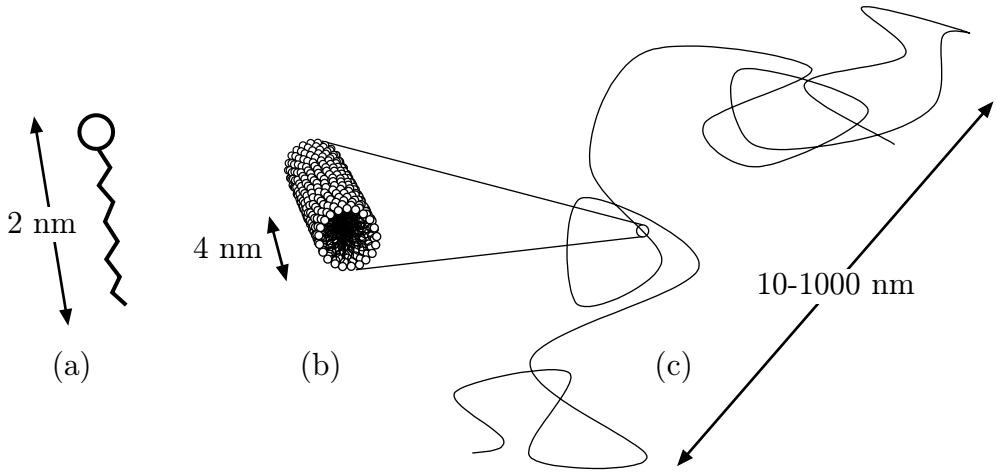

Figure 13: Surfactants and micelles at different length scales. (a) Surfactant molecule with hydrophillic head group and polar tail. (b) Cross section of a cylindrical micelle with the hydrocarbon tails shielded from the water by the polar head groups at the surface. (c) Random coil formed by a long cylindrical wormlike micelle.

rounding water. They do this by forming a sphere, for example, with all the tails on the inside of the sphere and all the polar heads at the surface of the sphere where they are in contact with the water. They can accomplish the same thing by forming other shapes as well, including cylinders, lamellae, and other more complex structures. Which structure forms depends on the surfactant concentration, the size of the head group relative to the tail, and the surfactant and solvent interactions. A cylindrical micelle is illustrated schematically in Figure 13.

The question of whether aggregates form or not involves a competition between energy and entropy. When aggregates form, the overall energy is reduced because the surfactant tails are shielded from the water. However, the formation of aggregates reduces the number of possible configurations and decreases the entropy. At low concentrations, entropy almost always wins and there are no micelles. As the concentration in increased, however, energetic considerations become increasingly important such that micelles begin to form above the cmc.

We are interested in cylindrical wormlike micellar solutions. These are systems where the shape of the surfactant head group, size of the tail, and interactions favor the formation of *cylindrical* aggregates. These cylinders can grow very long and flexible such that they resemble a long linear polymer chain. The basic differences between wormlike micelles and polymers are: (1) micelles typically have a diameter of about 4 nm, or about ten times greater than a typical polymer and (2) micelles are dynamical entities whose length is determined by equilibrium process; by contrast, the length of a polymer is fixed at the time of synthesis. The dynamical nature of wormlike micelles has several important ramifications. First, the distribution of the length L of wormlike micelles is thought to be broad, typically exponential [$P(L) \sim \exp(-L/\langle L \rangle)$]. Moreover, $\langle L \rangle$ in general increases with surfactant concentration. Thus, as surfactant concentration increases, the mean size of micelles increase leading to a situation where different micelles begin to overlap. As for conventional polymers, at concentrations above the overlap concentration c^*, these is a dramatic increase in viscosity and in the concentration dependence of the

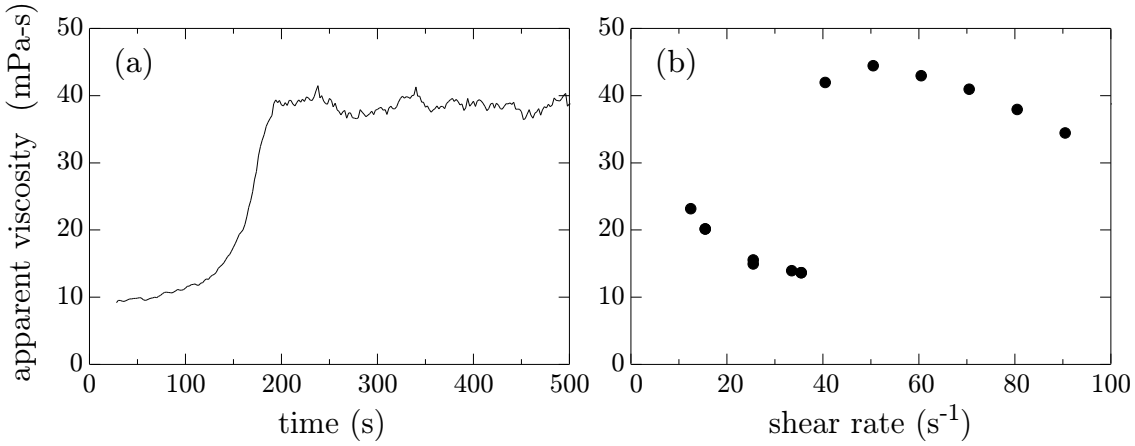

Figure 14: Basic rheology illustrating shear-thickening in solutions of wormlike micelles. (a) Slow increase in the viscosity measured after the application of a steady shear rate of approximately 80 s^{-1}. (b) Long-time steady-state measured viscosity exhibiting sharp increase above a critical shear rate of approximately 37 s^{-1}.

viscosity. A second important consequence of the dynamical nature of micelles is that they spontaneously break and reform in equilibrium. The rate at which this process occurs depends on the scission energy and the temperature; external disturbances such as shear flow can be expected to alter this process.

The specific systems we are concerned with here are ionic wormlike micelles formed from CTAB (cetyltrimethylamonium bromide) or closely related surfactants and NaSal (sodium salicylate), typically at or near a 1:1 molar ratio. NMR measurements reveal that when the CTAB forms cylindrical micelles in the presence of NaSal, the NaSal is incorporated into the micelle at nearly a 1:1 molar ratio. This means that the micelle has both positively and negatively charged ions, resulting from the disassociation of Br^- from the CTAB and Na^+ from the NaSal. This leaves a highly ionic solution where Coulomb interactions are likely to be important.

The basic shear-thickening rheology which interests us is illustrated in the two plots in Figure 14. In Figure 14(a) we show the response of a wormlike micellar solution to the sudden application of a steady shear rate. At first, nothing unusual occurs, but after tens of seconds the measured viscosity begins to rise until, after approximately 200 s, the system reaches a steady state plateau with a viscosity which is about 3 times larger than the viscosity of the original solution. The long-time steady-state viscosity obtained by repeating this experiment for different shear rates yields the data plotted in Figure 14(b). The most striking feature of these data is the existence of a critical shear rate $\dot{\gamma}$ above which shear thickening is observed and below which nothing extraordinary happens. This shear-thickening is observed for concentrations well below the overlap concentration c^* up to concentrations which are 2-3 times c^*.

3.2 Light scattering microscopy and rheology

Shear-thickening systems such as those discussed above have proven notoriously difficult to understand. One problem that was not well appreciated until recently is that such

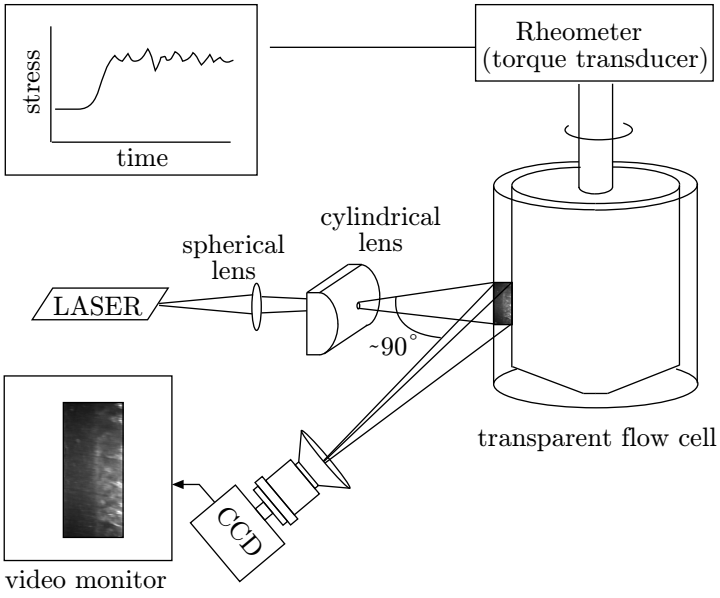

Figure 15: Experimental setup for light scattering microscopy.

systems frequently become spatially inhomogeneous on length scales comparable to the sample dimensions when they undergo a shear-thickening transition. When this occurs, the system can develop large-scale bands with different rheological properties. Thus, conventional macroscopic rheological measurements alone are not sufficient to understand the mechanical behavior of the system; one must be able to probe the spatial structure as well. Moreover, since such transitions often exhibit slowly evolving rheological changes accompanied by simultaneous structural changes, in becomes paramount to have a means for making *simultaneous* rheological and structural measurements.

Because of these concerns, we developed a transparent Couette cell rheometer and a light scattering technique for following rheological and structural changes in shear-thickening systems as they occur. Our apparatus is illustrated schematically in Figure 15. The sample is contained between two concentric quartz cylinders having diameters on the order of 25 mm and a gap between them of approximately 1 mm. A portion of the sample is illuminated by a sheet of laser light formed by passing the laser beam through a spherical and then a through a cylindrical lens as illustrated in Figure 15. The laser beam is directed radially inward towards the cell such that the illuminated volume has a width determined by the gap, is several millimeters high, and is about 50 μm thick. Light scattered through approximately 90° from this sheet of light is collected by a CCD camera such that an image of the scattering volume is formed on the CCD array. Regions of the sample which scatter light more strongly than other regions will appear brighter on the image. The resolution of the image is about 30 μm. At this resolution, an equilibrium sample is expected to be spatially homogeneous and therefore should exhibit uniform brightness across the illuminated volume.

In Figure 16, we show measurements of the transient effective viscosity of a micellar solution along with a succession of images obtained from our light scattering microscope. The left sides of the images correspond to the inner cylinder and the right sides to the outer cylinder of the Couette cell. After about 73 s, a bright region appears on the left

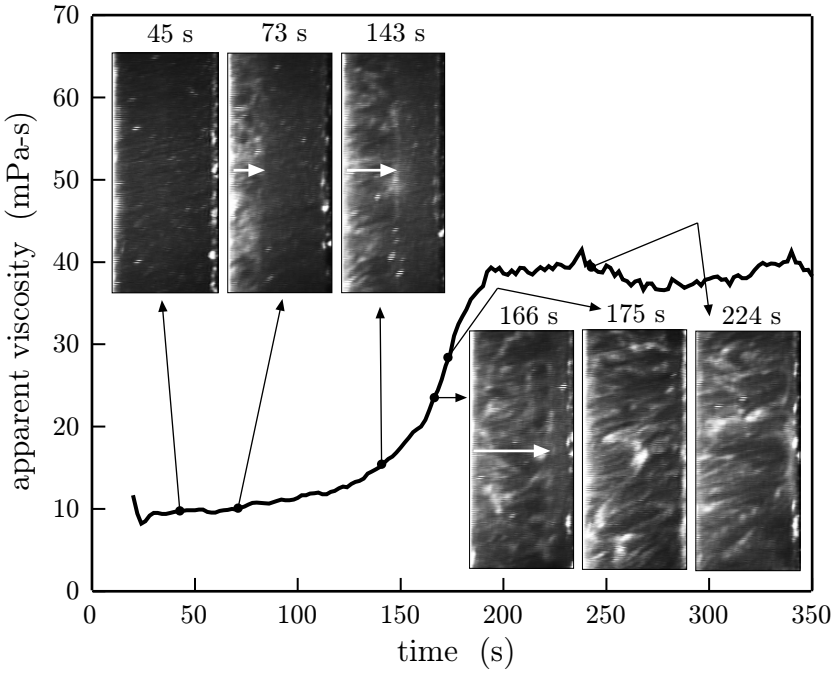

Figure 16: Effective viscosity vs. time after the commencement of shear flow. Data obtained at constant average shear rate. Images obtained at a succession of times show the growth of another phase as a region of increased scattering (brighter) which proceeds from the inner cylinder (left side of images) and grows towards the outer cylinder (right side of images). White arrows indicate the progression of the interface of the bright phase.

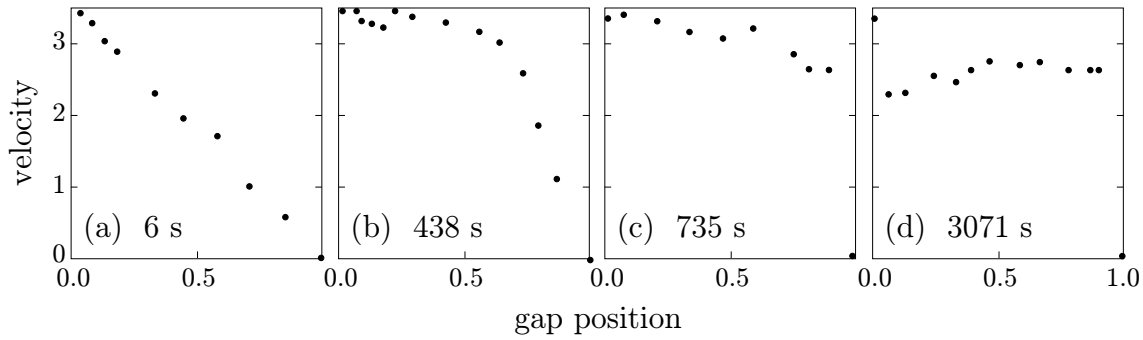

Figure 17: Velocity profiles in a Couette cell at 4 times after the commencement of shear flow. The inner cylinder is on the left (0.0) and the outer cylinder is on the right (1.0) in each of the plots. The numbers at the lower left corners indicate the time in seconds that have past after the commencement of shear flow.

side of the image just as the apparent viscosity begins to increase. As time proceeds, the measured viscosity increases and the bright region moves to the right towards the outer cylinder such that in fills an ever increasing fraction of the gap. Eventually, the bright phase appears to fill the entire gap and that all the shear is confined to a rather narrow gap. It also appears that the bright phase is more viscous than the dark phase.

If one of the two phases which appears in Figure 16 is more viscous than the other, then the velocity profile will not be constant across the gap. To investigate this possibility, we measure the velocity profile across the gap of the Couette cell using our light scattering microscopy apparatus. To effect these measurements, we rotate the plane of the sheet of laser light incident on the cell by 90° about the axis along the direction of propagation of the laser beam (see Figure 15. Thus, the sheet of light is oriented horizontally across the gap rather than vertically as in the previous measurements. We then seed the sample with a very small concentration of polystyrene microspheres and follow their motion in time as the traverse the illuminated sheet. By measuring the distance that each particle moves in successive video frames (30 frames/s), we are able to map out the velocity profile across the gap of the Couette cell. Figure 17 shows the results of such a measurement for an experiment in which a steady shear flow is applied to an equilibrium sample. The velocity profile is shown at 4 different times. Immediately after the commencement of shear flow, the velocity profile is linear across the gap as can be seen in Figure 17(a); thus, the velocity gradient is constant. The subsequent velocity profiles shown in Figure 17(b)-(d) reveal that the velocity gradient in the bright phase is much smaller than in the dark phase near the outer portion of the cylinder; that is, the bright phase is more viscous than the dark phase. In fact, to within the experimental precision, the velocity gradient in the bright phase is zero. Thus, we refer to the bright phase as a "gel." We emphasize, however, that our referring to it as a gel is simply a matter of convenience as the experiments strictly reveal only that the velocity gradient within the bright phase is very small. After about 10 minutes, the gel appears to fill the gap and all the flow is confined to a narrow slip layer next to the outer cylinder as can be seen in Figure 17. Later on, a slip layer appears at the inner cylinder as well although we do not wish to focus on such features here.

With the picture provided by our measurements of a gel growing from the inner cylin-

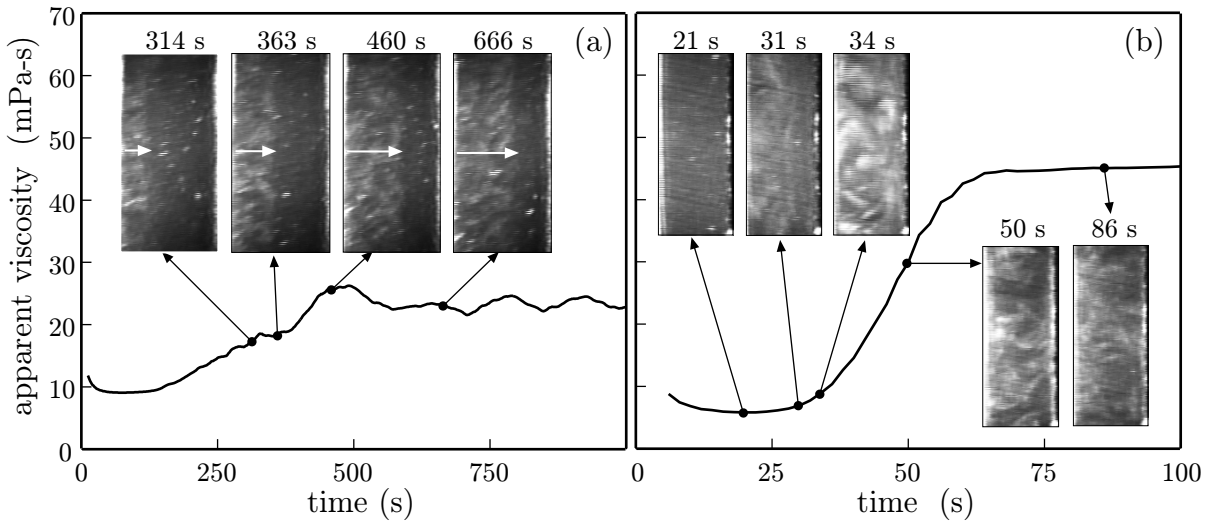

Figure 18: Effective viscosity vs. time after the commencement of shear flow. Data obtained at constant shear stress. Images obtained at a succession of times. (a) Stress = 0.6 Pa: White arrows indicate the progression of the interface of the bright phase as it grows from the inner cylinder. (b) Stress = 1.6 Pa: White phase appears homogeneously throughout the gap without a visible interface.

der and a few simple assumptions, we can already begin to understand some of the qualitative features of the discontinuous jump in the apparent viscosity. First, we see that the gel only begins to grow when a certain critical shear rate $\dot{\gamma}_c$ is exceeded. Consider then what happens when a shear rate $\dot{\gamma}_0 > \dot{\gamma}_c$ is applied to a sample which has been at equilibrium. We note, first of all, the stress in a Couette cell is greatest at the inner cylinder (we shall explain this in greater detail a little further on). Thus, it is not surprising that the gel begins to form at the inner cylinder. Since there is essentially no flow in the gel, and the average shear rate across the gap of the Couette cell is held constant, the shear rate $\dot{\gamma}_1$ in the remaining liquid must increase such that $\dot{\gamma}_1 > \dot{\gamma}_0 > \dot{\gamma}_c$. Thus, even more gel is formed. We might expect this process to continue until the surfactant available to form gel from the fluid phase is exhausted. In this way the gel phase can grow across the cell and cause the observed increase in the apparent solution viscosity.

Suppose that instead of keeping the shear rate constant that we keep the stress constant in our experiments. Thus, we apply a steady stress to a well rested sample and follow what happens to the rheology and structure of the sample. The results of one experiment where we hold the stress fixed at 0.6 Pa is shown in Figure 18. Initially after startup, the rheology and light scattering images look similar to those obtained under constant shear rate; the apparent viscosity increases as the viscous phase grows from the inner cylinder. An important difference, however, is that the gel phase stops short of the outer cylinder and remains in approximately the same position indefinitely. Thus, the gel and liquid phases can coexist at steady state for a constant applied stress.

If the experiment is repeated at the higher stress but still less than 1.2 Pa, the data are qualitatively similar to those obtained at 0.6 Pa and displayed in Figure 18 with the apparent viscosity increasing in proportion to the growth of the gel phase across the gap. At a stress of 1.2 Pa, the gel phase appears to fill the gap, just as in the case for constant

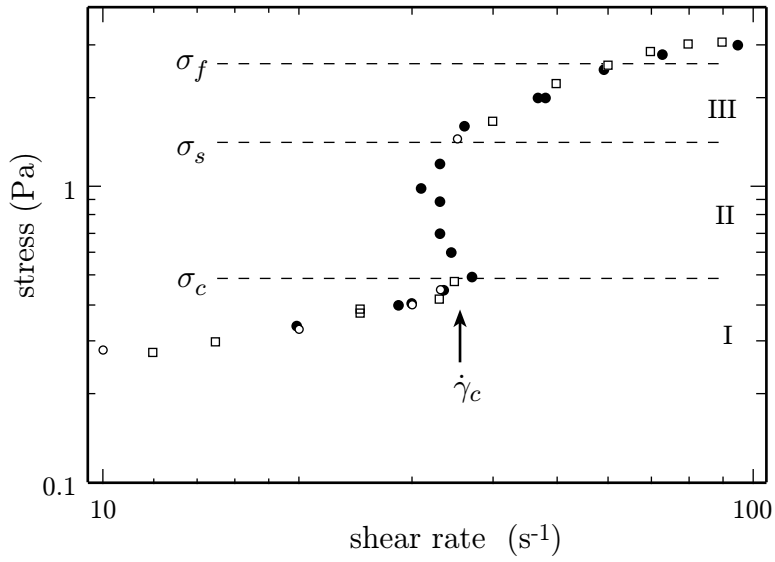

Figure 19: Steady state stress vs. average shear rate for data obtained under constant shear rate (open symbols) and constant stress (closed symbols).

shear rate. Once again, there is a very thin slip layer near the outer cylinder.

The situation changes somewhat when the experiment is repeated at higher stresses. Consider the data in Figure 18 obtained for a startup experiment performed at a constant stress of 1.6 Pa. In this case, the bright phase begins to appear after approximately 30 s but without any readily visible interface just as the apparent viscosity begins to rise. Indeed, by the time 34 s have passed, the bright phase is clearly visible throughout the gap but with only about a 20% rise in the apparent viscosity. As time passes, the apparent viscosity increases dramatically. Meanwhile the bright phase continues to fill the gap but its brightness appears to decrease somewhat in intensity. Thus, it appears that in contrast to data obtained at lower shear rates, at these higher shear rates the bright viscous phase nucleates homogeneously throughout the gap in small isolated droplets. As time progresses, these droplets connect and percolate throughout the gap causing the dramatic observed increase in the apparent viscosity. This interpretation of the data is also consistent with the observed brightness of the gel phase which is brightest around 34 s before the apparent viscosity has risen significantly. At this stage, the isolated droplets create large *fluctuations* in the concentration of surfactant. When the droplets of gel phase begin to interconnect, the fluctuations in concentration are reduced thus reducing the strength of the light scattering.

Figure 19 summarizes the behavior of the shear thickening behavior discussed this far. Note that there is a range of stresses between the critical stress σ_c and a higher stress σ_s where there exist steady states under controlled stress but not under controlled shear rate. These data correspond to the situation represented in Figure 18(a) where the gel and fluid phases coexist and both occupy a finite fraction of the gap. It is clear from the data in Figures 19 and 18 that the shear thickening seems to be better characterized by a critical shear *stress* rather than a critical shear *rate*. As can been seen in Figure 19, the average shear rate actually *decreases* when the system begins to shear thicken. Moreover, inside the gel, the shear rate is essentially zero. If it were the shear rate that controls the

formation of gel, then the gel would immediately dissolve upon formation because of the low shear rate inside the gel. Nevertheless, the gel remains. Note, however, that under all circumstances, the gel phase is only observed when the shear stress is greater than a critical shear stress σ_c as shown in Figure 19. Thus, the data strongly suggest that it is the shear stress and not the shear rate which controls determines the overall steady state of the system. The reader should be cautioned that this does not mean that the shear rate does not play any role in the kinetics of the nucleation and growth of the gel. It would seem, however, that the shear rate cannot act as a state variable for the long time steady behavior of the system.

The determinative role of stress is also evident in the cases where homogeneous rather than heterogeneous nucleation occurs. The main point here is simply that stress decreases as r^{-2} in a Couette cell. This follows from the fact that the torque must be balanced at every point in the gap. (The torque Γ is given by $\Gamma = rF$, where r is the radial distance from the axis of the Couette cell of a point in the gap and F is the force at that point. Since the force is related to the stress by $\sigma = F/(2\pi rh)$, where h is the height of sample in the gap $\sigma = \Gamma/(2\pi r^2 h)$ or $\sigma \propto r^{-2}$.) Thus, when the applied stress is near the critical stress, gel can only be nucleated where the stress is greatest – near the inner cylinder. When the stress in increased so that the stress is well above the critical stress throughout the gap, gel nucleates everywhere. While this is an appealing argument and probably at least partially correct, it must also be pointed out that the shear rate also decreases with radius, though with the weaker dependence of $\dot{\gamma} \sim r^{-1}$. For this and reasons previously discussed, one should not ignore the role of the shear rate in nucleation.

Thus far we have examined only the formation of the gel phase upon the commencement of shear flow. We can also ask what happens if, after a steady state has been reached, the shear rate is suddenly decreased to a value below the critical shear rate. In Figure 20 we show the results of several experiments in which the shear is suddenly decreased after the system has achieved a steady state at a shear rate well above the critical shear rate. In each experiment, the stress falls immediately by an amount which is linearly proportional to the decrease in the applied shear rate. This essentially instantaneous response is followed by a slower decrease in stress which can last several minutes or longer. In the first experiment, labeled (a) in Figure 20, the shear rate is suddenly decreased to a shear rate just a little greater than the critical shear rate. In this case, the gel remains intact and reaches a new steady state in about 100 s. When the shear rate is decreased to a value just below the critical stress, as shown in trace (b) in Figure 20, the stress appears to come to a new steady state at a point along the upper branch of the steady state curve shown in the inset (open circle). The system remains there for a few minutes before relaxing to the lowest stress on the steady state curve consistent with the applied shear rate (open square). In this state, the there is no gel. The data shown in trace (c) are similar to trace (b) though there is no obvious plateau as the stress relaxes to the low-stress state where there the gel has disappeared. Finally, when the shear rate is reduced to a value well below the range of shear rates where the steady-state curve is multivalued, the system once again relaxes fairly rapidly (within a few minutes) to its fluid gel-free state.

At the present time, the microscopic origin of shear thickening in these micellar systems is unknown. Various mechanisms have been suggested, the most developed of which is based on the idea that alignment of the micelles by the imposed flow causes the length of

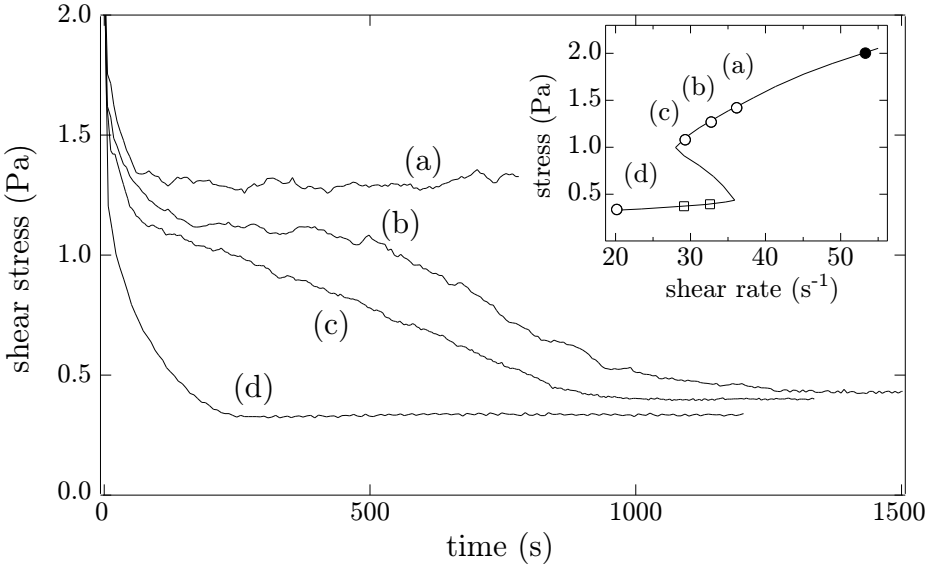

Figure 20: Quench experiments showing the response of the stress after a sudden decrease in shear rate. The system is prepared at a steady state shear rate of $\dot{\gamma}_0 = 44$ s^{-1} as indicated by the solid circle in the inset; the shear rate is then suddenly reduced to one of four lower shear rates indicated by the open circles and squares (see text).

the micelles to grow and to thereby increase the viscosity of the solution. Here, the basic idea has to do with a competition between entropy, which favors many short micelles over fewer longer micelles, and end cap energy, which seeks to minimize the number of micelles ends by forming fewer long micelles. The basic problem is that these theories produce only a mild shear thickening which is much smaller than that observed in experiments. These theories do not take into account the Coulomb interactions which are thought to be important in these systems because of the high degree of ionized species which are typically present in micellar solutions which shear thicken. Other suggestions have been offered as well, including a very interesting proposal involving the existence of closed micellar loops which are broken by shear flow. Presently, there is insufficient experimental evidence which strongly points to any particular theory.

Recently, there has been some progress in developing phenomenological theories which seem capable of reproducing much of the observed rheological behavior, including coexisting phases of a very viscous and less viscous phase under controlled stress. No microscopic mechanism for shear thickening is proposed in these models. Instead, these models posit the existence of a shear-induced phase transition along with an equation of motion for the interface between the two phases. Then, by employing simple constitutive equations for the rheological behavior and enforcing conservation of mass, one can reproduce much of the observed phase and rheological behavior of these systems, including re-entrant rheological curves similar to Figure 19 and discontinuities in the steady-state stress observed under constant shear rate. These models are significant because they can significantly limit the kinds of phase behavior possible, and thus can serve as a guide to the development of more sophisticated microscopic models. In this way, they resemble descriptions of equilibrium systems based on classical thermodynamics rather than statistical mechanics.

In concluding this section, we summarize the most significant results of these exper-

iments. First is the observation that shear thickening occurs by the nucleation of a new viscous phase. At shear rates and stresses just above $\dot{\gamma}_c$ and σ_c, the nucleation of the new phase in inhomogeneous and the system divides itself into macroscopically distinct regions of high and low viscosity. Second, shear stress rather than shear rate seems to be the more useful variable for describing the steady state of the system. Third, the shear-thickening transition seems to have the character of a first order phase transition. One should exercise caution, however, in applying equilibrium concepts such as phase transitions to systems and processes which are manifestly nonequilibrium. Nevertheless, for these systems the concept of a nonequilibrium phase transition seems to have some value.

Finally, it is useful to emphasize the utility of augmenting rheological measurements with structural measurements in systems which shear thicken. Indeed, simply by learning that these systems divide themselves into two distinct phases when they shear thicken, we have made significant progress towards our ultimate understanding of them.

4 Yielding and rearrangements in glassy emulsions

Fragile materials are characterized by a high degree of sensitivity to external forces and typically yield under very mild shear stresses. In most cases, the response of the material is elastic up to some yield stress beyond which the response is more complex, depending upon the system under consideration. In this section, we consider the response of one realization of such a material, namely emulsions, and study the structural rearrangements which occur when such as system is strained beyond its elastic limit. Before discussing the specific experiments, we provide a brief review of emulsions and their properties.

4.1 Emulsions

Emulsions are multicomponent systems which in their most basic form consist of three components: oil, water, and a surfactant. In fact, the two liquid components need not be oil and water, but can be any two liquids which are mutually insoluble (or which at most exhibit only very limited mutual solubility). Nevertheless, the vast majority of emulsions consist of water and some insoluble oil.

Emulsions are usually formed by mechanical mixing which creates a dispersion of oil droplets in a continuous background of water or a dispersion of water in a background of oil. The latter system is often called an "inverse emulsion." The smallest droplet size that can be achieved by mechanical mixing is typically about 0.1 μm. Such a mixture is not in equilibrium, however, and will demix unless measures are taken to suppress the subsequent coalescence of droplets. Suppressing coalescence is the role of the surfactant which, when mixed with the oil and water, goes to the interface between the droplets and the surrounding fluid. In some cases, the surfactant is electrically charged which results in a repulsive interaction between droplets. In other cases, the surfactant provides a steric or entropic barrier between droplets. In either case, the surfactant provides an effective repulsive interaction which acts as a barrier to coalescence by keeping the droplets from coming into contact. Thus, emulsions are kinetically stabilized against coalescence and do not represent the lowest energy state of the system. Normally, the lower energy state

consists of a system which is completely phase separated into macroscopic regions of oil and water with the surfactant dissolved in one of the phases, and perhaps existing as micellar solution. Alternatively, the system may form a thermodynamically stable microemulsion, in which case it can be difficult to maintain the systems as a nonequilibrium emulsion. Thermodynamically stable microemulsions differ from emulsions in that they consist of much smaller droplets (typically about 10 nm), are thermodynamically stable, and can usually form spontaneously without the addition of mechanical energy. Nevertheless, our interest here is focused on emulsions which are metastable and which, with proper selection of materials, can remain stable indefinitely.

When prepared by mechanical mixing, emulsions usually have a wide distribution of droplet sizes. Numerous methods have been developed for producing emulsions with a high degree of monodispersity. For example, various fractionation schemes have been developed by which a polydisperse emulsion can be successively divided into fractions consisting of particles all within a fairly narrow range of diameters. With some effort, samples with 10% polydispersity can be achieve in this manner. Other schemes, mostly mechanical, also exist whereby emulsions can be produced with polydispersities in the 10-30% range. These schemes require more specialized equipment but are capable of producing much greater quantities of monodisperse material. In the experiments we discuss in this section, the emulsions have a polydispersity of about 10%. This level of polydispersity prevents the emulsion droplets from forming an ordered crystal. Thus, the emulsions discussed here are amorphous at all concentrations.

When the volume fraction ϕ of droplets in an emulsion is not too high, emulsions behave very similarly to colloidal dispersions of solid particles. They are subject to the same thermal forces, for example, and exhibit Brownian motion just as do solid colloidal particles. The situation changes, however, when the volume fraction of droplets approaches and exceeds random close packing. For nearly monodisperse spheres, random close packing occurs at volume fraction ϕ_{rcp} of about 0.63. For $\phi \ll \phi_{rcp}$, emulsion droplets exist as isolated spheres. But as ϕ approaches ϕ_{rcp}, increasingly less space is available to each particle. For $\phi > \phi_{rcp}$, no more room is available and particle motion is arrested. It is still possible to mechanically deform the system, however, because the droplets themselves are deformable. We briefly review the mechanical behavior of random close packed emulsions below.

4.2 Mechanical properties of random close packed emulsions

For sufficiently small strains, one expects a random close packed emulsion to exhibit linear viscoelastic behavior. That is, one expects the system to respond elastically, but not without some viscous dissipation arising from shearing of the liquid in the emulsion. Such behavior can be characterized by a complex frequency dependent elastic shear modulus $G(\omega)$. To understand the physical meaning of $G(\omega)$ we consider the following simple experiment. Suppose an emulsion is confined between two parallel plates which are spaced a distance apart which is much greater than the droplet diameter (a spacing of ~ 1 mm is typical). The top plate is moved back and forth sinusoidally producing a time-dependent shear strain across the sample which is given by $\gamma(\omega, t) = \mathrm{Re}[\gamma_0 \exp(i\omega t)]$ where ω is the frequency and γ_0 is the strain amplitude. One then measures the time-dependent stress $\omega(t)$ on the bottom plate which for a linear viscoelastic material can be written

as $\sigma(\omega, t) = G(\omega)\gamma(\omega, t)$ Because the system exhibits both viscous dissipation and elastic response, the stress is in general not completely in phase with the applied strain. Thus, $G(\omega)$ is complex and is written as $G(\omega) = G'(\omega)+G''(\omega)$, where $G'(\omega)$ characterizes the in phase elastic response of the system and $G''(\omega)$ characterizes the out of phase dissipative or viscous response of the system.

At small strains, close packed emulsions deform elastically like any elastic solid with an elastic modulus $G'(\omega) = G'_0$ which is independent of frequency. By contrast, the dissipative response which is characterized by the loss modulus $G''(\omega)$ becomes smaller as the frequency is reduced reflecting the fact that viscous dissipation depends on the *velocity* gradient rather than the *displacement*. In the limit low frequencies, $G''(\omega) = \eta\omega$ where η is the zero-frequency (or zero-shear-rate) viscosity of the emulsion.

At low strains, measurements of $G'(\omega)$ and $G''(\omega)$ are independent of the strain amplitude γ_0 as expected for a linear viscoelastic material. As the strain is increased, however, the response becomes nonlinear and amplitude dependent signaling the onset of yielding and plastic flow. Mason *et al.* [6] have studied the linear and nonlinear rheology of concentrated disordered emulsions as well as yielding and flow. As expected they find normal linear viscoelastic behavior at low strain amplitudes consistent with an elastic solid as described above. Above a concentration-dependent strain amplitude, they find that the emulsions do yield. They also find that there is a dramatic increase in the dissipation associated with the onset of nonlinear behavior and yielding. One expects that this increased dissipation is associated with irreversible rearrangements of droplets. Unfortunately, the rheological measurements do not provide any direct measurement of such droplet motions. For this, we turn to light scattering.

4.3 Light scattering in emulsions in an oscillatory shear flow

The basic phenomenon we wish to investigate is the irreversible movement of emulsion droplets subjected to an oscillatory shear flow; the basic idea is to use dynamic light scattering. As discussed previously in Section 2.2.2, a light scattering measurement performed on a sample undergoing oscillatory shear flow leads to a series of echoes in the temporal correlation function of the scattered light. Although the experiments described in Section 2.2.2 were discussed in the context of single light scattering, all the concepts apply equally well to multiple light scattering, that is, to DWS. The only pertinent difference is that multiple light scattering is much more sensitive to particle motion and can therefore detect much smaller irreversible particle movements. Therefore, we expect to obtain data qualitatively similar to that displayed in Figure 11.

In Figure 21, we show a schematic of the experimental setup for a DWS transmission experiment. Light from a laser is multiply scattered by the emulsion contained between two glass slides. For the case shown, multiply scattered light which is transmitted through the sample is detected and sent to an electronic correlator. The glass slides are roughened to insure that the emulsion does not slip when the upper slide is oscillated back and forth. Backscattering DWS experiments are carried out using the same cell but multiply scattered light is collected from the same side of the sample on which it is incident.

In Figure 22, we show data obtained from an emulsion subjected to an oscillatory shear flow with a strain amplitude of $\gamma_0 = 0.010$ and frequency of 57.8 Hz ($\phi_{oil} = 0.85$). The figure shows the initial decay of the correlation function and the first echo. Between

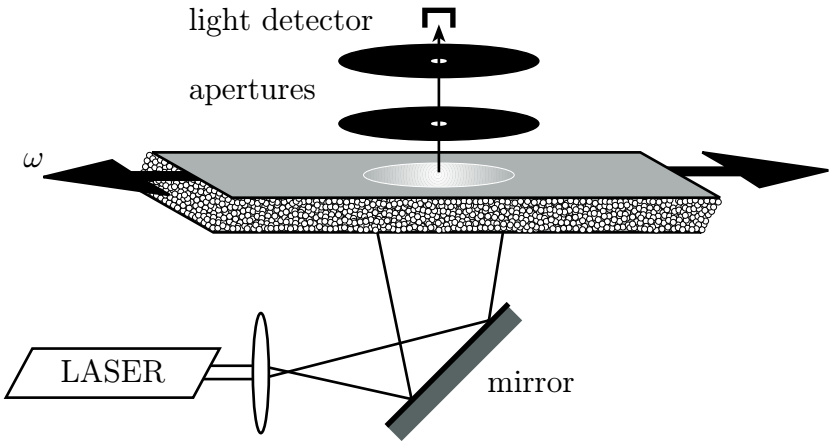

Figure 21: Schematic of DWS transmission measurement of sheared emulsion. Coherent light from a laser is expanded and directed towards the bottom glass plate on which the emulsion is placed. The upper glass plate is moved back and forth using a precision piezo-electric device. Apertures assure that light from on the order of one speckle is collected by the detector.

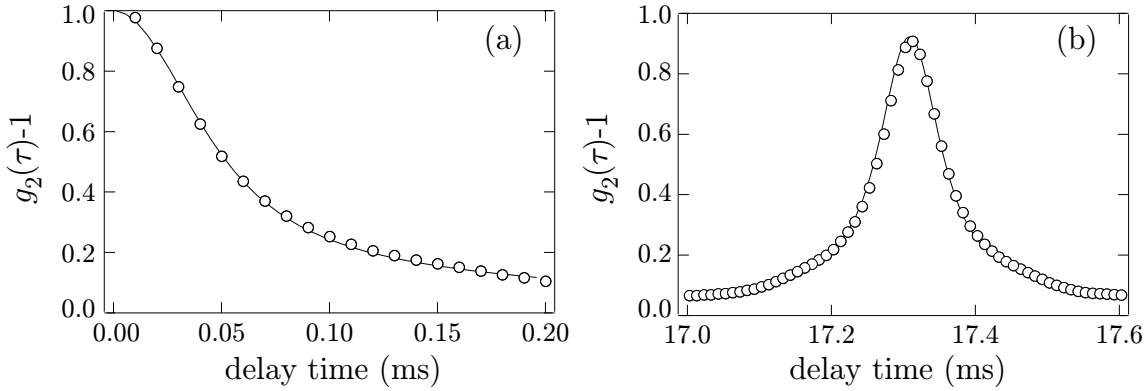

Figure 22: Temporal correlation function obtained using diffusing-wave spectroscopy on an emulsion undergoing oscillatory flow. (a) Initial decay of the correlation function arising from the shearing motion. (b) First echo in correlation function centered at a delay time of one period of the imposed oscillating shear flow.

these two features, the correlation function is essentially zero. Note that the widths of the initial decay and the echo are much narrower than the delay time between them. The width of the peaks is set by the characteristic shear rate $\gamma_0\omega$ and the thickness of the cell [7]. Because of the narrow widths of the peaks, it is essential that the clocks running the correlator and the shear flow be synchronized. This can be accomplished, for example, by using the clock for the correlator as the master clock to which the shear flow is synchronized using a phase-locked loop. Alternatively, two separate clocks may be used if they are both sufficiently stable over the duration of the experiment.

To extract useful information from the correlation functions we measure, we need an expression for the correlation function. Recall that in Section 2.2.3 we derived expressions for $g_E(\tau)$ as an integral over light paths through the sample which had the form:

$$g_E(\tau) = \int_0^\infty P(s)\, e^{-x(\tau)s/l^\star}\, ds \ , \tag{45}$$

where x depended on the type of motion that the scatterers execute. For example, in Eq. (40), $x = (k^2/3)\langle \Delta r^2(\tau)\rangle$ where $\langle \Delta r^2(\tau)\rangle$ is the mean square displacement of the scatterers. For oscillating shear flow, it can be shown that this reduces to,

$$x(\tau,\tau_0) = \frac{1}{15}\left[kl^\star\left|\gamma(\tau+\tau_0)-\gamma(\tau_0)\right|\right]^2 \ , \tag{46}$$

where $\gamma(\tau_0)$ is the initial value of the strain [7, 8]. For oscillatory flow, the particle motion is not stationary but depends on which part of the strain cycle the systems is at. A typical electronic correlator, such as the one used in these experiments, calculates $g_I(\tau)$ from the data stream in a manner which essentially assumes the process producing the data is stationary. Thus, it continually updates the time τ_0 at which it starts calculating the correlation function. Therefore, to account for the fact that an oscillating shear flow is not stationary, we must integrate the theoretical correlation function over all initial values of the strain. This will allow comparison with data taken from the correlator. Thus, we substitute Eq. (46) into Eq. (45), and integrate the intensity correlation function over all initial strains (one oscillation period):

$$g_I(\tau) - 1 = \frac{\omega}{2\pi}\int_0^{2\pi/\omega} \left|g_E[x(\tau,\tau_0)]\right|^2 \, d\tau_0 \ , \tag{47}$$

The integral in Eq. (47) can be performed numerically to obtain the shapes of the correlation functions we measure. We determine the transport mean free path $l^\star$ by measuring the total transmitted intensity [2, 9].

As stated previously, $g_I(\tau)$ in insensitive to $l^\star$ in the transmission geometry and the initial decay of the correlation function essentially depends only on the strain amplitude γ_0 and frequency ω. Thus, we can compare our data to the theoretical expression given in Eq. (47) without any adjustable parameters. The result of this comparison is shown in Figure 22(a) where the circles represent the data from the experiment and the solid line the theoretical result obtained from Eq. (47). The agreement between theory and experiment is remarkable and confirms out theoretical description of the decay of the correlation function due purely to shear flow.

In writing Eqs. (46) and (47), we have assumed that there is no motion other than the affine displacement of scatterers with the applied strain. If this is the case, then the

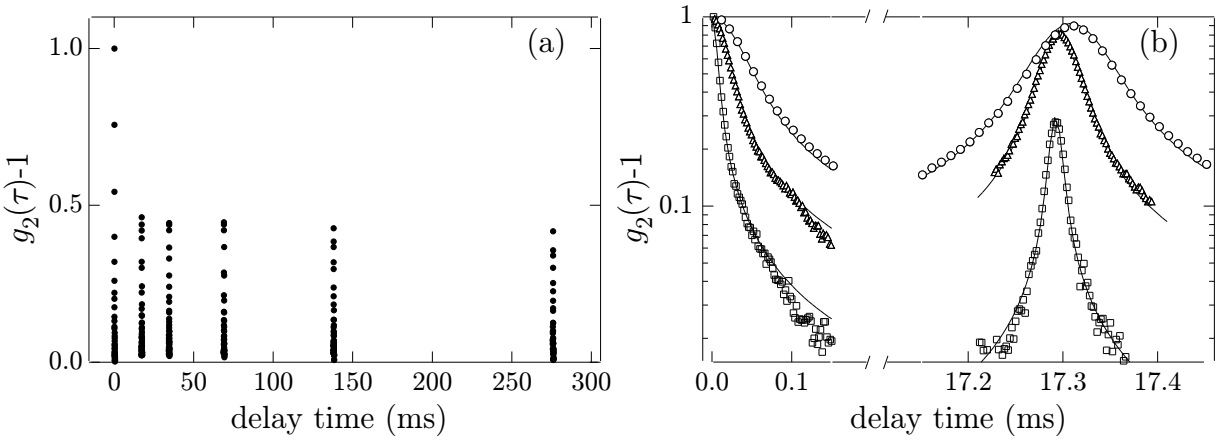

Figure 23: Temporal correlation function obtained using diffusing-wave spectroscopy on an emulsion undergoing oscillatory flow. (a) Correlation function showing initial decay and multiple echoes. The strain amplitude is $\gamma_0 = 0.05$. (b) Initial decay and first echo in correlation function on an expanded time scale. The strain amplitudes are $\gamma_0 = 0.01$ (circles), 0.02 (triangles), and 0.06 (squares). The use of slightly different strain frequencies leads to the slightly shifted peak positions of the echoes.

scatterers should all return to their exact same positions when the shear is reversed thereby causing an echo in the correlation function at a delay time of the period of oscillation. Furthermore, the shape of the echo should be governed by the same process that governs the initial decay discussed above. Thus, the shape of the echo should be described by Eqs. (46) and (47). In Figure 22(b) we show a fit of the data to Eqs. (46) and (47) where the only adjustable parameter is the echo height about which we have no *a priori* knowledge. Once again, the theory fits the data very well.

We now turn to the decay of the echo heights under the application of the oscillating shear. In Figure 23(a), we show a correlation function for a sinusoidal shear flow with a strain amplitude of $\gamma_0 = 0.05$. Because of technical limitations in the instruments used to calculate the correlation function from the experimental data train, only the first, second, fourth, eighth, and sixteenth echoes were determined in these experiments. The other echoes exist, as confirmed by other experiments, but were not determined in the measurement displayed. The first echo is less than unity, as expected, because of irreversible motion of at least some of the droplets. There is one quite unexpected feature of these data, however, and that is that *all the echos have the same height.* This is in stark contrast to the behavior illustrated in Figure 11 where the echo heights decayed exponentially consistent with particle diffusion. Indeed, light scattering experiments on colloidal suspensions under an oscillating shear exhibit the expected exponential decay [10].

Although all the echoes have the same height for a given strain amplitude γ_0, the height of the echoes decrease with increasing γ_0, as shown in Figure 23(b). For all strain amplitudes, however, the echo height is constant for as large of delay times as we can measure. We also note that this same behavior is observed for backscattering DWS measurements as well.

The fact that the echoes to not decay after the first echo means that there is a finite

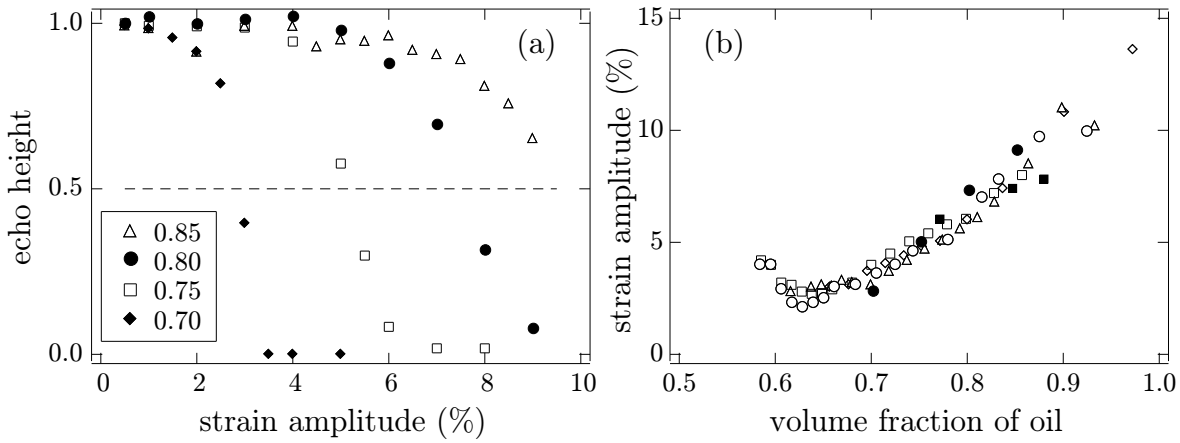

Figure 24: (a) Echo height from DWS backscattering experiments vs. strain amplitude for different volume fractions. (b) Comparison of the critical strain amplitude vs. volume fraction obtained from DWS measurements (solid symbols) to yield strains obtained from rheological measurements by Mason *et al.* [6] (open symbols).

fraction of the emulsion which undergoes reversible periodic motion. If this were not the case, there would not be any echoes. It also means that there is another fraction of the emulsion for which undergoes irreversible motion. That is, the trajectories of some fraction of the emulsion droplets are chaotic. This is why the echo heights are less than unity. Finally, the fact that the echo heights do not change in time means that these two fractions of emulsion droplets are disjoint sets. If a droplet undergoes a reversible trajectory after one shear cycle, then it does so indefinitely. Similarly, if a droplet undergoes an irreversible trajectory after one shear cycle, then it does no indefinitely. Thus, under oscillatory shear *the system partitions itself into fragile regions which are fluid-like and elastic regions which are solid-like.* Furthermore, these regions maintain their identity and integrity over time.

The dependence of the echo heights on strain amplitude is shown in Figure 24. This plot shows that the echo height decays monotonically as a function of increasing strain amplitude. Thus, an the volume fraction of droplets that rearrange under strain increases as the amplitude of the strain increases.

Mason *et al.)* [6] found using rheological measurements that the emulsion yields above some critical value of the strain amplitude. To make contact with their measurements, we plot the data they obtained for the yield strain vs. volume fraction of droplets in Figure 24(b). In the same Figure, we also plot the volume fraction at which the echo heights drop to one half their initial value. While this criterion is somewhat arbitrary, the good agreement between the two data sets support the idea that yielding is associated with particle rearrangements in the emulsion.

To obtain a quantitative measure of the volume fraction of emulsion that undergoes rearrangements we must analyze the shape of the correlation function and the echo heights in more detail. Basically, there are three contributions to the shape of the correlation function: (1) the decay arising from the oscillatory straining motion which we have already discussed, (2) the spontaneous decay of the correlation function caused by Brownian motion, and (3) droplet rearrangements caused by the oscillating strain. The spontaneous decay arising from Brownian motion is observable only at the lower volume fractions,

where their remains some room for the particles to move. This contribution to $x(t)$ is given by $(k^2/3)\langle \Delta r^2(t) \rangle$ where $\langle \Delta r^2(t) \rangle$ is the mean square displacement caused by Brownian motion and can be determined from the decay of $g_2(\tau)$ in the absence of shear.

The contribution to the decay of the correlation function arising from rearrangements can be determined in the following way [11]. In the absence of a rearrangement event, we assume that there is no decay of the height of the echo. That is, the length of a light path through the sample is exactly the same as it was one oscillation period ago unless the path intersects a region in the sample that undergoes a rearrangement. In the case that it does intersect a region that has undergone a rearrangement, the phase of that path is completely randomized. This assumption is justified by the fact that the droplet sizes are comparable to the wavelength of light and any rearrangement of even a small group of droplets is virtually certain to change the path length through the sample by at least one wavelength. Thus, the height of the echo is simply determined by the fraction of paths that have not been randomized after a delay time τ where τ is an integral number of oscillating periods. If the number of rearrangements of a given size a occur randomly at a rate R per unit volume, then the rate at which rearrangements occur within a light path α is proportional to the product of R and the volume swept out by the light path $sl^{\star 2}$, since $l^\star$ is the shortest length scale over which one can describe the transport of light within the diffusion approximation. In addition, α will scale as $a^3/l^{\star 3}$ since larger rearrangement events will randomize more paths. Thus, $\alpha \approx R(sl^{\star 2})(a^3/l^{\star 3}) = (a^3 R)(s/l^\star)$. This means that the contribution to the decay of the correlation function of paths of a given length s is $\exp(-\alpha\tau) = \exp[-(a^3R)(s/l^\star)\tau]$. This can be written in simpler form by noting that at any given delay time, the volume fraction Φ of the sample that has undergone an irreversible rearrangement is $\Phi = aR^3\tau$. Thus, in Eq. 45, to within factors of order unity, $x(\tau) \approx \Phi(\tau)$.

Putting together the three contributions to the decay of the correlation, we obtain

$$x(t) = \frac{1}{3}k^2\langle \Delta r^2(t) \rangle + \frac{1}{15}\left[kl^\star \left|\gamma(\tau+\tau_0) - \gamma(\tau_0)\right|\right]^2 + \Phi(\tau) \tag{48}$$

Substituting this into Eq. 45, we can use this result to extract from the echo height the volume fraction which has undergone irreversible rearrangements. Note that in general, the volume fraction of sample which has undergone irreversible rearrangements can have a time dependence, and is written explicitly as having one in Eq. 48. The fact that the echo heights do not change in time simply reflects the fact that the volume fraction which undergoes irreversible rearrangements remains constant in time.

In Figure 25, we plot the volume fraction of emulsion Φ that has rearranged as a function of strain amplitude γ_0. Data obtained in both transmission and backscattering are plotted. At large strain amplitudes, there is some discrepancy between the transmission and backscattering measurements suggesting that the volume fraction of emulsion which undergoes irreversible rearrangements increases near the walls of the sample. As expected, the emulsions which have a lower volume fraction of droplets undergo more rearrangements at a given strain amplitude than do emulsions with a higher volume fraction of droplets. By comparing our measurements of $\Phi(\gamma_0)$ shown in Figure 25 to the measurements of yield strain by Mason *et al.* [6] we estimate that yielding occurs in these emulsions when approximately 4% of the emulsion droplets have undergone irreversible rearrangements.

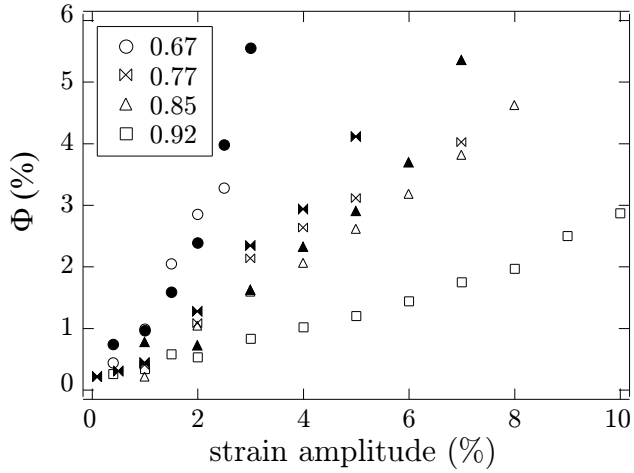

Figure 25: Volume fraction Φ of emulsion droplets which undergo irreversible rearrangements vs. strain amplitude. The solid symbols were obtained from backscattering data and the open symbols from transmission data. The volume fraction of droplets for each data set is indicated in the legend.

5 Acknowledgments

The work described in this article represents collaborations with many people over a number of years. In particular, the sections on light scattering represents the collaborations with P.M Chaikin, D.J. Durian, D.A Weitz, X.-l. Wu, and A.J. Yodh, as well as productive interactions with many others too numerous to mention here. The shear thickening work reflects collaborations with P. Boltenhagen, E. Matthys, and Y.T. Hu. I have also benefited greatly from discussions with J. Goveas and P. Olmstead, and David Lu on this topic. Finally, the section on sheared emulsions represents a collaboration with P. Hébraud, F. Lequeux, and J.P. Munch.

References

[1] B. J. Berne and R. Pecora, *Dynamic light scattering : with applications to chemistry, biology, and physics* (Wiley, New York, 1976).

[2] D. Weitz and D. Pine, "Diffusing-Wave Spectroscopy," in *Dynamic Light Scattering: The Method and Some Applications*, Vol. 49 of *Monographs on the physics and chemistry of material*, W. Brown, ed., (Oxford University Press, Oxford, 1993), pp. 652–720.

[3] M. E. Cates and S. J. Candau, "Statics and dynamics of worm-like surfactant micelles," J. Physics: Cond. Mat. **2,** 6869–6892 (1990).

[4] I. Wunderlich, H. Hoffmann, and H. Rehage, "Flow birefringence and rheological measurements on shear induced micellar structures," Rheol. Acta **26,** 532–542 (1987).

[5] H. Rehage and H. Hoffmann, "Shear induced phase transitions in highly dilute aqueous detergent solutions," Rheol. Acta **21,** 561–563 (1982).

[6] T. G. Mason, J. Bibette, and D. A. Weitz, "Yielding and Flow of Monodisperse Emulsions," J Colloid Interface Sci **179,** 439–448 (1996).

[7] X.-l. Wu, D. Pine, P. Chaikin, J. Huang, and D. Weitz, "Diffusing-Wave Spectroscopy in a Shear Flow," J. Opt. Soc. B **7,** 15–20 (1990).

[8] P. Hébraud, F. Lequeux, J. Munch, and D. Pine, "Yielding and rearrangements in disordered emulsions," Phys. Rev. Lett. **78,** 4657–4660 (1997).

[9] D. J. Durian, "Penetration depth for diffusing-wave spectroscopy," Appl. Opt. **34,** 7100–7105 (1995).

[10] X. Qiu, H. Ou-Yang, D. Pine, and P. Chaikin, "Self-Diffusion of Interacting Colloids Far from Equilibrium.," Phys. Rev. Lett. **61,** 2554–2557 (1988).

[11] D. Durian, D. Weitz, and D. Pine, "Multiple Light-Scattering Probes of Foam Structure and Dynamics," Science **252,** 686–688 (1991).